Comparison of 1*A* GeV ^{197}Au+C data with thermodynamics: The nature of the phase transition in nuclear multifragmentation

R. P. Scharenberg,[1] B. K. Srivastava,[1] S. Albergo,[2] F. Bieser,[6] F. P. Brady,[3] Z. Caccia,[2] D. A. Cebra,[3] A. D. Chacon,[7,a] J. L. Chance,[3] Y. Choi,[1,b] S. Costa,[2] J. B. Elliott,[1,c] M. L. Gilkes,[1,d] J. A. Hauger,[1,e] A. S. Hirsch,[1] E. L. Hjort,[1] A. Insolia,[2] M. Justice,[5,f] D. Keane,[5] J. C. Kintner,[3,g] V. Lindenstruth,[4,h] M. A. Lisa,[6,i] H. S. Matis,[6] M. McMahan,[6] C. McParland,[6,d] W. F. J. Müller,[4] D. L. Olson,[6] M. D. Partlan,[3,c] N. T. Porile,[1] R. Potenza,[2] G. Rai,[6] J. Rasmussen,[6] H. G. Ritter,[6] J. Romanski,[2,j] J. L. Romero,[3] G. V. Russo,[2] H. Sann,[4] A. Scott,[5] Y. Shao,[5,k] T. J. M. Symons,[6] M. Tincknell,[1,l] C. Tuvé,[2] S. Wang,[5] P. Warren,[1,m] H. H. Wieman,[6] T. Wienold,[6,h] and K. Wolf[7,n]

(EOS Collaboration)

[1]*Purdue University, West Lafayette, Indiana 47907*

[2]*Universitá di Catania and Istituto Nazionale di Fisica Nucleare-Sezione di Catania, I-95129 Catania, Italy*

[3]*University of California, Davis, California 95616*

[4]*GSI, D-64220 Darmstadt, Germany*

[5]*Kent State University, Kent, Ohio 44242*

[6]*Nuclear Science Division, Lawrence Berkeley National Laboratory, Berkeley, California 94720*

[7]*Texas A&M University, College Station, Texas 77843*

(Received 7 June 2000; published 1 October 2001)

Multifragmentation MF results from 1*A* GeV Au on C have been compared with the Copenhagen statistical multifragmentation model (SMM). The complete charge, mass, and momentum reconstruction of the Au projectile was used to identify high momentum ejectiles leaving an excited remnant of mass *A*, charge *Z*, and excitation energy E^* which subsequently multifragments. Measurement of the magnitude and multiplicity (energy) dependence of the initial free volume and the breakup volume determines the variable volume parametrization of SMM. Very good agreement is obtained using SMM with the standard values of the SMM parameters. A large number of observables, including the fragment charge yield distributions, fragment multiplicity distributions, caloric curve, critical exponents, and the critical scaling function are explored in this comparison. The two stage structure of SMM is used to determine the effect of cooling of the primary hot fragments. Average fragment yields with $Z \geqslant 3$ are essentially unaffected when the excitation energy is $\leqslant 7$ MeV/nucleon. SMM studies suggest that the experimental critical exponents are largely unaffected by cooling and event mixing. The nature of the phase transition in SMM is studied as a function of the remnant mass and charge using the microcanonical equation of state. For light remnants $A \leqslant 100$, backbending is observed indicating negative specific heat, while for $A \geqslant 170$ the effective latent heat approaches zero. Thus for heavier systems this transition can be identified as a continuous thermal phase transition where a large nucleus breaks up into a number of smaller nuclei with only a minimal release of constituent nucleons. $Z \leqslant 2$ particles are primarily emitted in the initial collision and after MF in the fragment deexcitation process.

DOI: 10.1103/PhysRevC.64.054602 PACS number(s): 24.10.Lx, 25.70.Mn, 25.75.−q

[a]Present address: Space Systems/Loral, Palo Alto, CA 94202.

[b]Present address: Sun Kwun Kwan University, Suwon 440-746, Republic of Korea.

[c]Present address: Nuclear Science Division, Lawrence Berkeley National Laboratory, Berkeley, CA 94720.

[d]Present address: Mission Research Corp., Santa Barbara, CA 93102.

[e]Present address: Augusta State College, Augusta, GA 30910.

[f]Present address: Brookhaven National Laboratory, Upton, NY 11793.

[g]Present address: St. Mary's College, Morage, CA 94575.

[h]Present address: Universität Heidelberg, Heidelberg, Germany.

[i]Present address: Ohio State University, Columbus, OH 43210.

[j]Present address: The Svedberg Laboratory, University of Uppsala, S-751-2 Uppsala, Sweden.

[k]Present address: Crump Institute for Biological Imaging, UCLA, Los Angeles, CA 91776.

[l]Present address: MIT Lincoln Laboratory, Lexington, MA 02420.

[m]Present address: Naval Research Laboratory, Washington, D.C. 20375.

[n]Deceased.

I. INTRODUCTION

Multifragmentation (MF) is the dominant decay mode in heavy ion reactions when the excitation energy is comparable to the nuclear binding energy. The recent use of 4π detectors capable of observing a substantial fraction of the particles and fragments emitted in a given interaction has been invaluable in furthering the elucidation of this complex phenomenon [1–6]. Several review articles of MF have been published in recent years [7–9].

One of the most complete MF experiments to date has been that performed by the EOS collaboration for the ^{197}Au on C system [10–17]. The use of seamless detectors such as the EOS time projection chamber coupled with the multiple sampling ionization chamber (MUSIC II) permitted the observation of practically all the charged particles and fragments emitted in each event, ranging from protons to heavy fragments. Full reconstruction was therefore possible for a large fraction of the events. The high energy asymmetric collision of a 1*A* GeV projectile on a light target is uniquely favorable for the kinematic separation of the initial nuclear collision and the subsequent MF transition. This data set permitted us to establish that MF occurs following the expansion of a remnant formed with charge *Z*, mass *A*, and excitation energy E^* after the prompt ejection of high momentum light particles [11,13]. We have applied model independent methods used in the study of critical phenomena to extract the value of several critical exponents [10,12]. The critical scaling function, which describes the behavior of the nuclear remnant near a critical point, was determined [14]. In performing this analysis we were aided by percolation calculations [18,19], which served as a quantitative guide to the application of the methods developed for the study of critical exponents in small systems.

The EOS experiment was an outgrowth of earlier inclusive studies of MF in the interaction of Xe and Kr with high-energy protons [20–26]. In this work high precision counter techniques were used to obtain accurate information about the kinetic energy spectra of *isotopically* resolved nuclear fragments. The reduced Coulomb barrier seen in the fragment spectra indicated that nuclear fragments are emitted from an expanded nuclear system. Systematics of the fragment kinetic energy spectra also showed that the remnant was lighter than the target nucleus implying that *the nuclear remnant existed for a time* after the initial collision. The relative fragment yields of 63 isotopes could be understood using a thermal droplet model [27] with a free energy parametrization based on the semiempirical mass formula. For energy depositions of ~8 MeV per nucleon this multiisotope thermometer gave a freeze-out temperature of ~5 MeV. The systematic variation of the ''kinetic temperature'' (exponential slope parameter extracted from fragment kinetic energy spectra) as a function of the fragment mass also indicated that Fermi momentum in the remnant must play a significant role in the fragment formation process.

More speculative was the suggestion that the power law yield of the fragment masses $Y=A^{-\tau}$ with $\tau\sim 2.6$ observed in 50–400 GeV *p* on Xe collisions showed that nuclear fragmentation might give information about a possible ''liquid-gas'' thermal phase transition in charged nuclear matter [21]. Important support for this view came from the exclusive emulsion data of Waddington and Freier [28], which were analyzed by Campi to show that the conditional moments of the individual fragment events exhibited features characteristic of a critical transition [29,30]. The occurrence of thermal equilibrium in the MF process was strongly supported by the experiments of the ALADIN Collaboration, which showed that fragment yields were independent of the entrance channel when the data was scaled for projectile or target mass [1,31].

The above cited evidence for the formation of a substantially equilibrated remnant which expands prior to MF suggests that it would be appropriate to compare the EOS results with a thermal model in which MF occurs from an expanded state. Two widely used thermal multifragmentation models are the Copenhagen (SMM) [32] and Berlin (MMMC) [33] statistical treatments. These models differ in their parametrization of the expansion and in technical details but are similar in their thermodynamic approach. For very small systems both these microcanonical models predict the onset of a very inhomogeneous state at a definite excitation energy. This inhomogeneous excited state consists of a number of normal density fragments accompanied by a statistically insignificant number of nucleons. Subsequently these fragments cool by light particle emission. We present here a comparison of the EOS data with SMM. Several data and model comparisons have been made previously [34–42]. These comparisons seriously suffered from the fact that the experiments did not determine the *Z*, *A*, and E^* of the remnant. Instead, these Z,A,E^* values, which constitute the proper input to test models of MF, were obtained either by use of a dynamical first stage model [34,36], by using a comparison of some of the data with SMM to constrain them [35,37,39–41], or by more complex backtracing from fragment data [38,42]. A great advantage afforded by asymmetric reverse kinematics collisions is that they permit an accurate separation of the initial reaction phase from the subsequent decay of the excited remnant.

The use of SMM also permits us to examine several aspects of the EOS critical exponent analysis that are potentially problematic. The EOS results were obtained for fragments in their final, cold state. However, the fragments are presumably formed in an expanded hot state. In SMM the remnant is equilibrated, the fragments are formed in the hot system, then separate under the influence of the Coulomb force and undergo deexcitation. As has been noted elsewhere [41], the distribution of the hot, primary fragments may be affected by secondary decay. The difference between the two distributions could, in principle, affect the values of the critical exponents. Since SMM gives separate results for hot and cold fragments, the effects of secondary decay can be probed.

The EOS results indicate that the first prompt step leads to a distribution of remnants. The analysis groups these remnants according to the total charged particle multiplicity, *m*, which serves as the control parameter. Events characterized by a given multiplicity will generally include a range of remnant Z,A,E^* values. It has been noted that such event mix-

ing can affect the values of the critical exponents [43]. Furthermore, the use of multiplicity instead of temperature or excitation energy as the control parameter has been questioned [44,45]. Comparison of SMM results obtained for the experimental distribution of remnants with those obtained for a single remnant permits us to probe the importance of these effects.

This paper is organized in the following manner. Section II gives a brief summary of SMM and shows how the data determine the variable volume of SMM. Only a single adjustable parameter remains. Section III summarizes the properties of the experimental remnant distribution, which serves as the input data to SMM. The occurrence of radial expansion energy as part of the excitation energy is discussed in this section. The comparison between experimental and model results is presented in Sec. IV. The various factors that can affect the fragment yields, the extraction of critical exponents, and the critical multiplicity are considered in Sec. V. In Sec. VI, the physics of MF and the nature of the thermal phase transition in SMM as a function of the remnant mass and charge is explored. The identification of the order of a thermal phase transition for the MF of Au on C requires the use of the microcanonical equation of state. A summary of the results and our conclusions are given in Sec. VII.

II. THE SMM MODEL

SMM is a statistical description of the simultaneous breakup of an expanded excited nucleus into nucleons and hot fragments [32]. Individual fragments at normal nuclear density are described with a charged liquid drop parametrization. The free energy of a fragment $A,Z(Z\geqslant 3)$ is given by

$$F_{A,Z}=F_{\rm trans}+F_{\rm vol}+F_{\rm surf}+F_{\rm sym}+F_{\rm Coul} \tag{1}$$

and is used to determine the fragment formation probability. This solution explicitly assumes the inhomogeneous nature of the hot MF final state. Light fragments $Z<3$ may also be present in the hot MF final state. For the $Z\geqslant 3$ fragments, a quantum mechanical description is used for the temperature dependent volume, surface, and translational free energy of the fragments. The temperature independent parameters are based on the coefficients of the semiempirical mass formula. The critical temperature, at which the surface tension of neutral nuclear matter droplets would go to zero, is in the range suggested by infinite neutral nuclear matter calculations [46].

In SMM the translational free energy depends on the *free* volume. The free volume, V_f, can be expressed in terms of the volume of the multifragmenting system at normal nuclear density, $V_{\rm rem}$,

$$V_f=\chi V_{\rm rem}, \tag{2}$$

where the free volume parameter χ depends on the SMM fragment multiplicity according to the relation

$$\chi=\left[1+\frac{d}{R_0}(M^{1/3}-1)\right]^3-1, \tag{3}$$

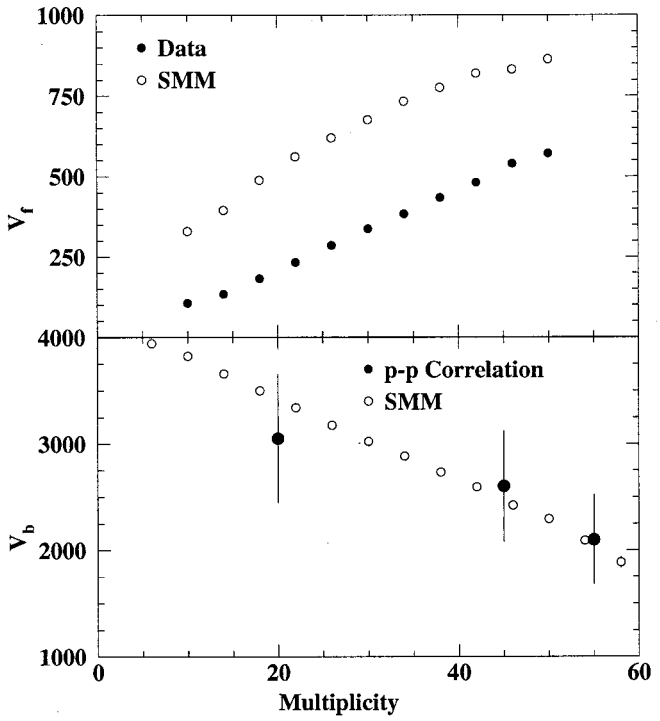

FIG. 1. (a) SMM free volume [Eq. (2)] and the experimental initial free volume [Eq. (4)] for the MF region. (b) SMM breakup volume and the experimental freezeout volume from p-p correlations. The variation in V_b is due to the decrease of the remnant mass. The remnant does not expand in compound nucleus events which occur at low multiplicity.

where $R_0=1.17A_0^{1/3}$ fm and M is the *charged plus neutral* hot fragment multiplicity. The crack width parameter, d, scales the magnitude of the multiplicity dependent free volume. The breakup volume V_b, which includes the volume of the fragments, is $V_b=(1+\kappa)V_{\rm rem}$, where κ is the Coulomb reduction parameter [32].

We have previously shown that energy deposition in the Au on C reaction is proportional to nucleons knocked out of the Au nucleus by quasielastic nucleon-nucleon scattering [13]. If we assume that the excited remnant initially is produced in the Au volume, then the experimentally determined *initial free volume* is given by

$$V_f^i=V_{\rm Au}(A_{\rm Au}-A_{\rm rem})/A_{\rm Au} \tag{4}$$

and the remnant volume is given by

$$V_{\rm rem}=V_{\rm Au}(A_{\rm rem}/A_{\rm Au}). \tag{5}$$

Proton-proton correlation experiments for the multifragmentation of 1*A* GeV Au on Au show that the freeze-out volume is $\sim 2V_{\rm Au}$, nearly independent of excitation energy and remnant mass and charge [47].

Figure 1(a) shows the SMM free volume V_f, and the initial free volume V_f^i as a function of the multiplicity. As expected, the SMM free volume V_f is about twice the initial free volume, consistent with the expansion from $V_{\rm Au}$ to $2V_{\rm Au}$. Note that the slopes of the V_f and V_f^i versus multiplicity curves track over the MF region.

TABLE I. Parameters in the SMM free energy expression.

	Fixed parameters	
W_0	Volume binding energy of cold nuclear matter	16 MeV
β_0	Surface tension of the cold nucleus	18 MeV
T_c	Neutral matter critical temperature	18 MeV
$\gamma_{\rm sym}$	Symmetry energy coefficient	25 MeV
d	Crack width parameter	1.4 fm
κ	Coulomb reduction parameter	2
	Single adjustable parameter	
ϵ_0	Inverse level density parameter	16 MeV

Figure 1(b) compares the breakup volume

$$V_b=(1+\kappa)V_{\rm rem}=(1+\kappa)(A_{\rm rem}/A_{\rm Au})V_{\rm Au} \qquad (6)$$

with the freeze-out volume from p-p correlations as a function of the multiplicity. The breakup volume V_b tracks the freezeout volume from the p-p correlation experiments. The freeze out volume calculated in our earlier publication [13] is different as it was obtained using initial volume of Au nucleus and not the remnant volume. Thus, experiment confirms the structure (M dependence) and scale (crack width parameter d) of the volume parameterization of SMM for the 1A GeV Au on C experiment. In addition to these experimental arguments, theoretical arguments based on BUU modeling of the nuclear collision [48] also suggest that the expansion of the remnant is energy dependent.

The remaining parameter is ϵ_0, the inverse level density parameter. The ϵ_0 values were determined by comparison of SMM with the various experimental fragment yield distributions and it was found that $\epsilon_0=16$ MeV. Thus the so-called standard values of all these parameters turn out to give the best agreement with the data. (See Table I.)

In SMM the primary fragments are propagated in their mutual Coulomb field and then undergo secondary decay. In the model successive particle emission from hot fragments with $A>16$ is assumed the deexcitation mechanism. The deexcitation of these fragments is treated by means of the standard Weisskopf evaporation model. Light fragments ($A<16$) deexcite via Fermi breakup. The lightest particles ($A<4$) can be formed only in their ground states and undergo no secondary decay. We have used a version of the model that incorporates only thermal degrees of freedom. Consequently, radial expansion or angular momentum are not included in this comparison between data and SMM.

III. THE INPUT DATA

A. Properties of the remnant

The reverse kinematics EOS experiment permitted the identification of charged projectile fragments $1\leqslant Z\leqslant 79$ in 1A GeV ^{197}Au on C interactions with high efficiency. The momenta of these fragments were measured and used to decompose the reaction into a prompt stage, in which high momentum $Z=1$, $Z=2$ fragments and neutrons are emitted, and a second stage involving the decay of the remnant left after this stage [13]. The analysis presented here is based on about 32 000 fully reconstructed MF events for which the total charge of the reconstructed Au system was found to be 79 ± 4. Average fragment mass values for a given Z were determined and used to reconstruct the MF final state mass A' of the charged fragments. The number of free neutrons in the MF final state is used in the determination of E^* by energy balance.

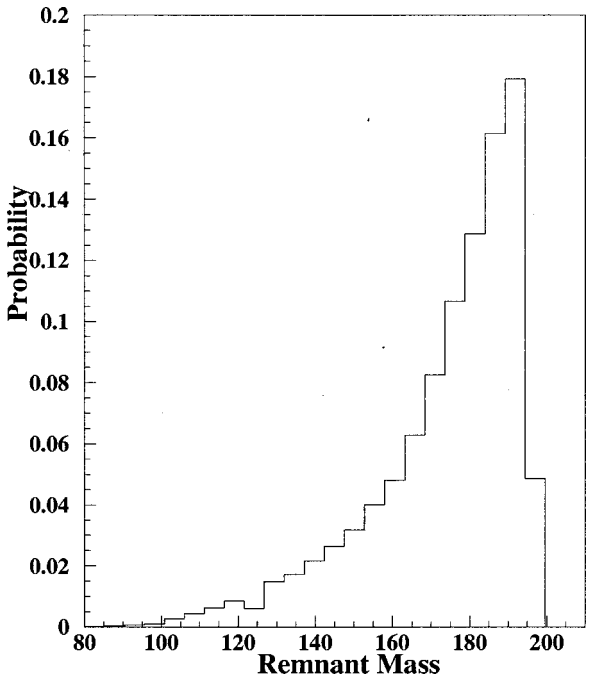

FIG. 2. Mass distribution of the experimental remnant.

The remnant resulting from the prompt stage can be characterized by Z, A, and E^*. We follow previous practice and report E^* on a per nucleon basis. The determination of these quantities has been described in detail elsewhere [13]. Figure 2 shows the mass distribution of the remnants.

The most probable mass is $A\sim190$. However, the distribution is broad and extends down to $A\sim100$. The E^* distribution is shown in Fig. 3(a). The distribution peaks at $\sim$2 MeV/nucleon but extends beyond 16 MeV/nucleon.

It should be noted that the data were obtained with a minimum bias trigger that eliminated some events with very low E^*. These events do not lead to MF. Figure 4 shows the variation of E^* and A with the total charged particle multiplicity m. These quantities vary in the opposite way with m, with E^* increasing with m, and A showing a concomitant decrease. At a given m there is a distribution in the values of A and E^*. For a given m, the width of the distribution in A increases from $\sim$1% to $\sim$13% while that of the E^* distribution is $\sim$25% over most of the multiplicity range [13].

B. The effect of nonthermal expansion

We have previously shown that some of the excitation energy of the remnant actually consists of nonthermal expansion energy, E_x [13,15]. The model input energy E_i is obtained by subtracting E_x from the excitation energy E^*.

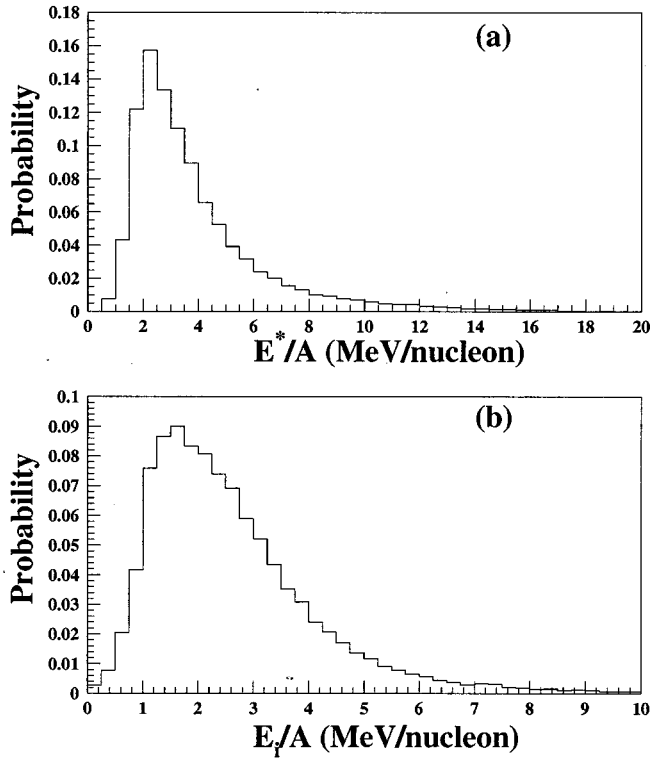

FIG. 3. Distribution of remnants as a function of (a) total excitation energy and (b) input excitation energy to SMM.

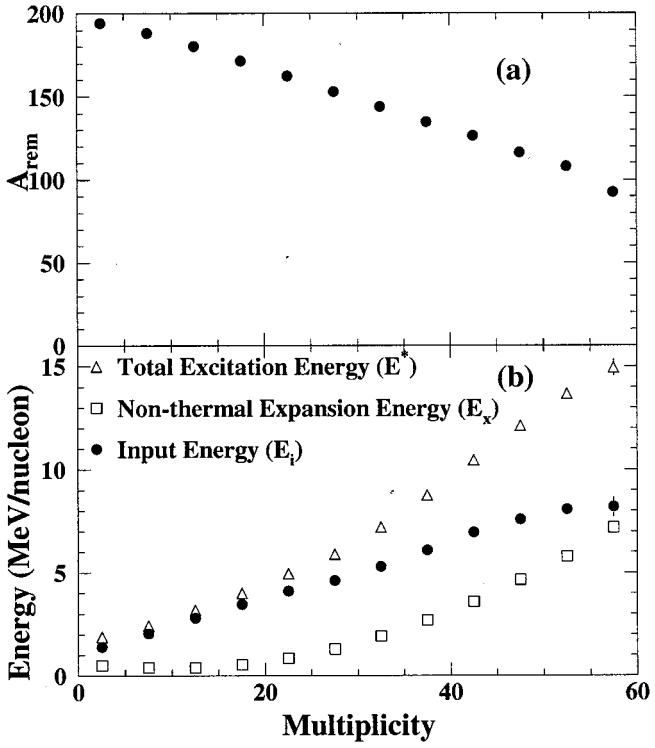

FIG. 4. Dependence on total charged particle multiplicity of some average properties of the experimental remnants: (a) mass, (b) total excitation energy (E^*), nonthermal expansion energy (E_x), and input energy (E_i). All energies are in MeV/nucleon.

Standard SMM does not include radial expansion and so only E_i must be used in the input data. Figure 4 shows the dependence of E_x and E_i on the multiplicity m. The expansion energy is very small for $m \lesssim 20$ but then increases sharply, becoming comparable to the input energy for the largest observed multiplicity, $m \sim 60$. The spectrum of E_i values is plotted in Fig. 3(b). The distribution peaks at slightly less than 2 MeV/nucleon and extends to ~10 MeV/nucleon.

The expansion energy was obtained as the difference between the sum of the measured charged fragment mean kinetic energies and the translational thermal and Coulomb energies of the fragments [13,49]. This procedure involves the use of the Albergo double isotope ratio thermometer [50] to determine the *isotopic temperature* T_a. This temperature determines the translational thermal energy per particle, which is $3/2T_a$. As shown in the next section, SMM then independently predicts the observed double isotope ratio. This self-consistency supports the validity of the E_i determination and permits a combined definitive test of the isotope ratio thermometer T_a and SMM.

Additional independent evidence for the presence of expansion energy in the data can be seen in a comparison of the mean transverse kinetic energies of fragments with the SMM predictions [49]. Figure 5 shows the results for Li-N fragments for five multiplicity bins: 1–9, 10–19, 20–29, 30–39, and 40–59. Generally good agreement is obtained for low multiplicities, as expected, because of the small contribution of the radial expansion energy for small m (see Fig. 4). The SMM transverse kinetic energy values decrease with increasing m.

In general, the SMM transverse energies are smaller than the experimental values. The trend in the SMM values is the result of two factors, both of which lead to a decrease in the translational kinetic energy with increasing multiplic-

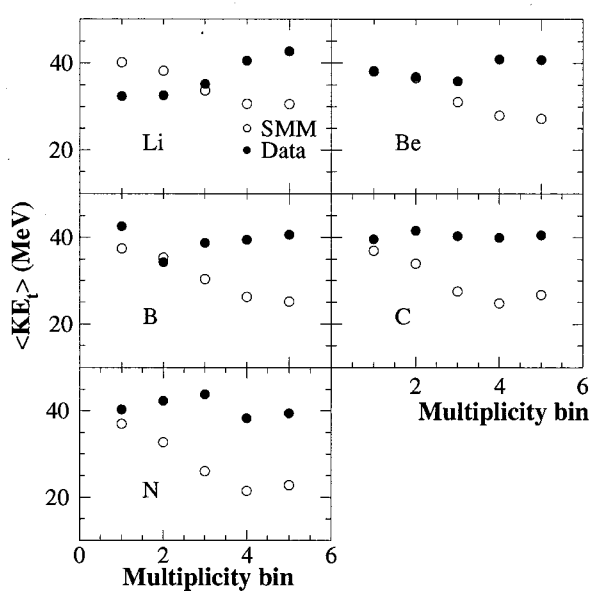

FIG. 5. Mean transverse kinetic energies of fragments as a function of nuclear charge. The multiplicity bins are 1–9, 10–19, 20–29, 30–39, and 40–59, respectively.

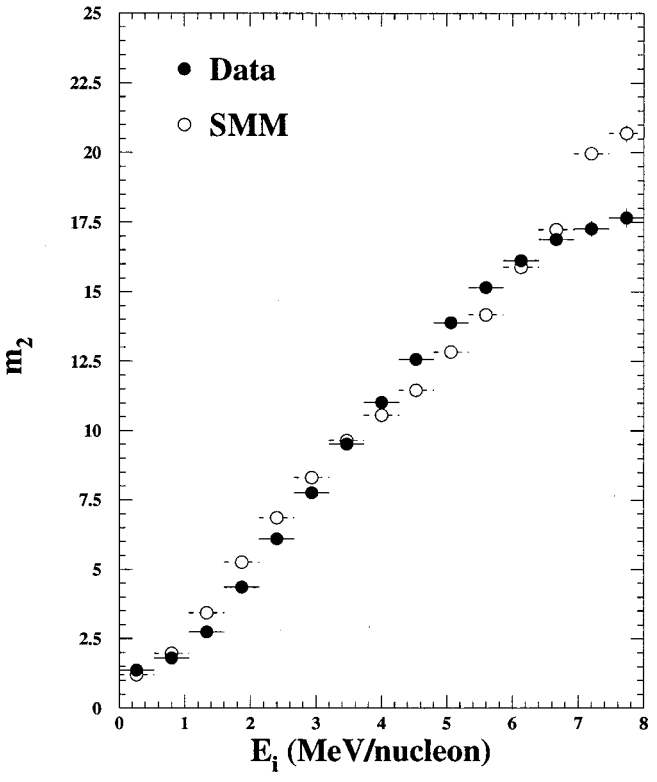

FIG. 6. Variation of second stage multiplicity with input energy.

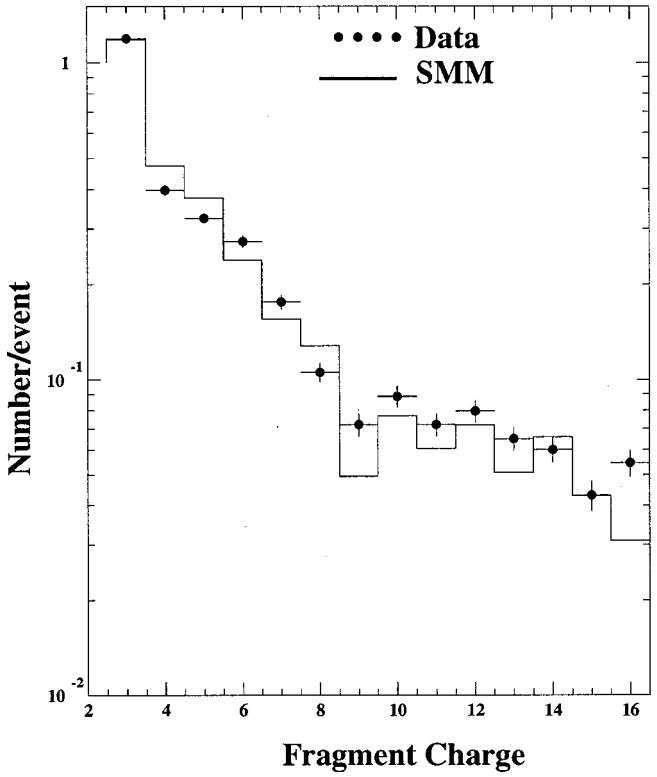

FIG. 7. Yield of fragments averaged over all m as a function of fragment charge.

ity: (1) the increase in the volume occupied by the fragments [32] and (2) the decrease in the average charge of the fragments. In particular, see Fig. 11, which shows the variation of the calculated and experimental charges of the largest fragment with m. SMM is in excellent agreement with experiment indicating that the reason for the discrepancy shown in Fig. 5 does not lie in the determination of the mutual Coulomb energy. Rather, the increasing contribution of nonthermal expansion to the experimental energies dominates the change in Coulomb energy. A similar discrepancy has been observed when another data set was used to compare SMM with the Berlin statistical model [33]. Here, too, the discrepancy was attributed to radial expansion energy [15].

IV. COMPARISON OF EXPERIMENTAL DATA WITH SMM

A single SMM calculation was performed for each of the 32 000 EOS events. The input data consisted of the Z, A, and E_i values of the remnants. The output of each SMM calculation gives the Z and A values of each fragment in its asymptotic cold state. The distribution of these MF products is used to make the comparisons presented in this section.

A. Fragment yield and multiplicity comparisons

Owing to the important role of multiplicity in the EOS experiment, we compare the SMM and experimental multiplicities at the outset. This comparison is made as a function of E_i. See Fig. 6. Since SMM does not include a prompt first stage, the SMM charged particle multiplicity is compared to the experimental second stage multiplicity, m_2. This quantity is obtained from m by subtracting event-by-event the prompt first stage multiplicity, m_1 [13]. The calculated and experimental m_2 distributions are in close agreement. Because of this agreement, SMM results will be plotted as a function of m in many subsequent comparisons with data. Here m will be the sum of SMM m_2 and experimental m_1 values.

The fragment yield distributions offer the most direct comparison between the data and SMM. Figure 7 shows the number of $Z=3-16$ fragments per event averaged over all multiplicities. Good agreement is obtained for nearly all the fragments and the overall trend of decreasing yield with increasing charge is well reproduced. Both data and SMM show that the yield of fluorine is suppressed relative to that of neighboring fragments. SMM indicates that this low yield reflects the influence of final state interactions on the primary fragments.

The individual fragment yields are plotted as a function of m in Figs. 8 and 9. SMM generally does an excellent job of reproducing the data except for the lightest fragments, where the model predicts too many fragments for large m. Both data and SMM show the characteristic rise and fall of the individual fragment yields as a function of m or E_i. Both of these distributions were used in the statistical analyses which extract the power law and critical scaling behavior. The average value of the total number of intermediate mass fragments $\langle \mathrm{IMF} \rangle$ as a function of m is shown in Fig. 10.

The yield of IMF's increases to $\sim$4.4/event at $m \sim 48$ and decreases for larger m. This behavior is reproduced by SMM,

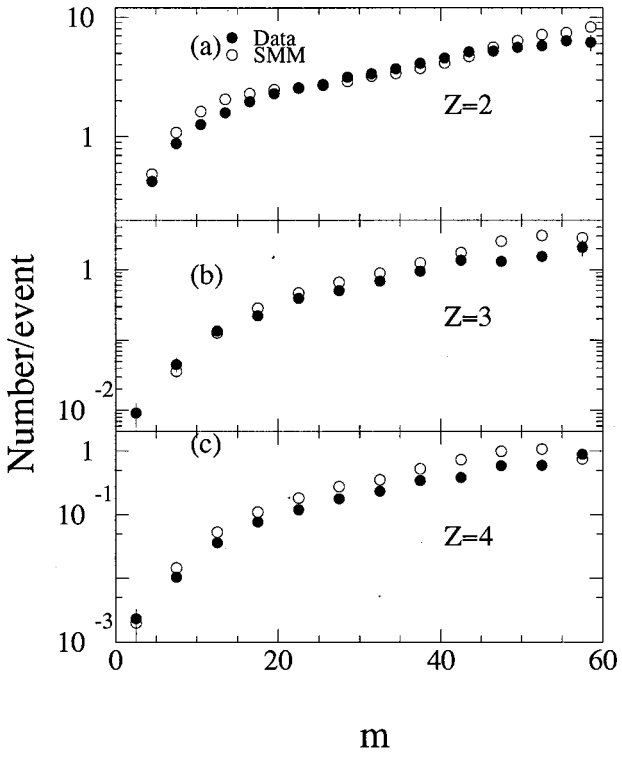

FIG. 8. Average yield of fragments, for $Z=2,3,4$ as a function of m.

although the number of IMF's at the peak is somewhat overestimated. This difference is a consequence of the above discrepancy between data and SMM for Li and Be fragments at large m. Figure 11 shows the average value of the charge of the largest fragment in the distribution, $Z_{\max}$. SMM gives the best agreement with the data using $\epsilon_0=16$ MeV.

We have previously [13] obtained from the data the isotopic temperature T_a [50] on the basis of ^{2}H/^{3}H and ^{3}He/^{4}He

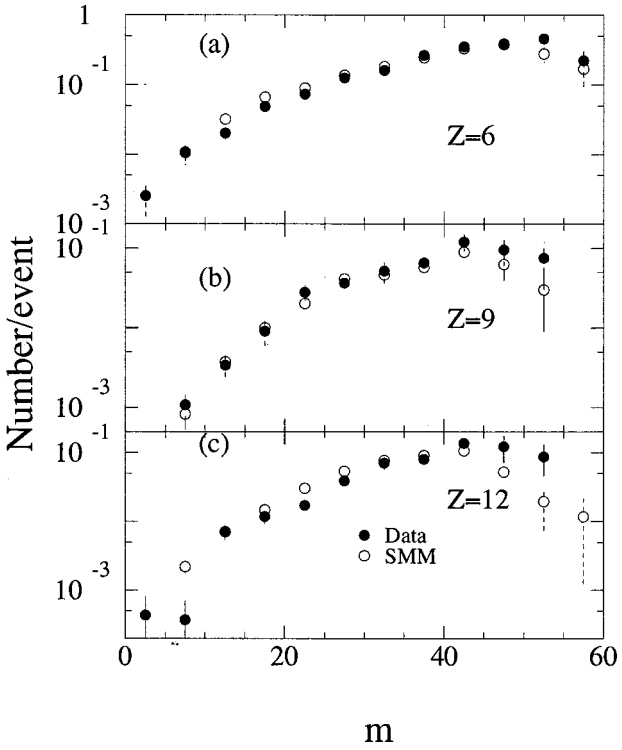

FIG. 9. Average yield of fragments, for $Z=6,9,12$ as a function of m.

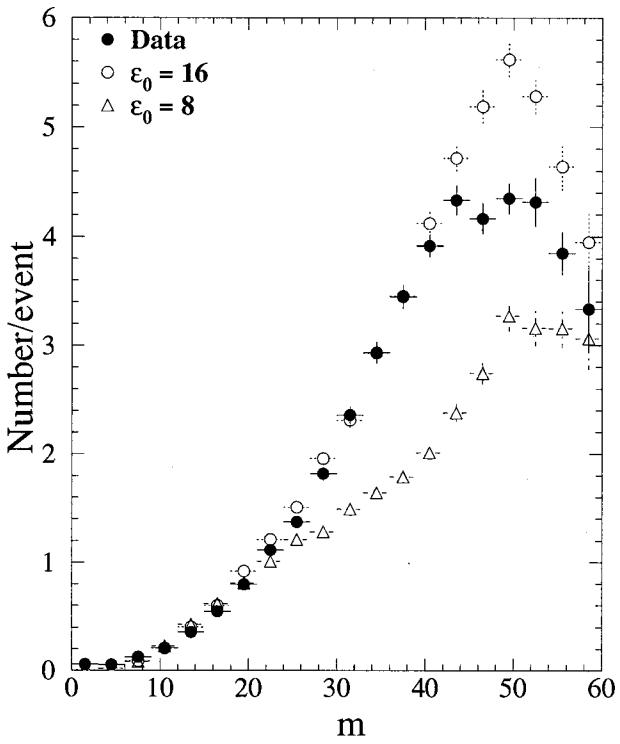

FIG. 10. Average yield of intermediate mass fragments for $Z=3-30$ as a function of m. SMM results are shown for $\epsilon_0=16$ and $\epsilon_0=8$.

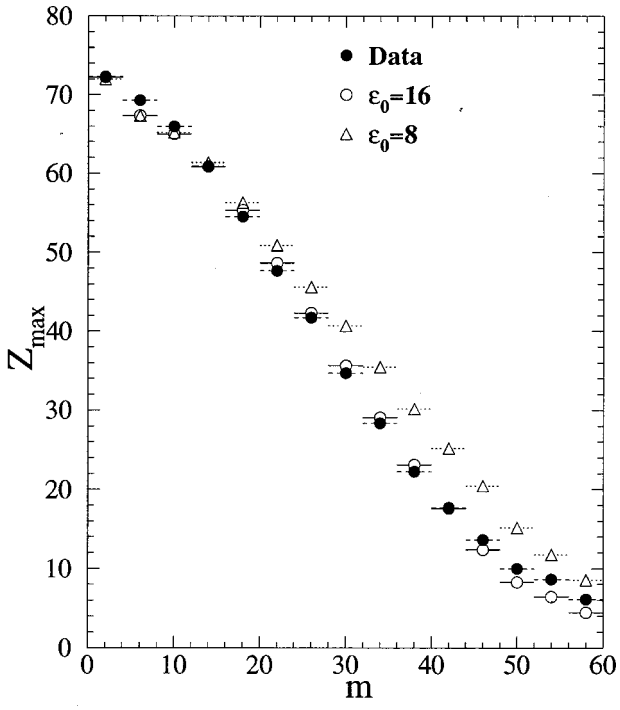

FIG. 11. Charge of the largest fragment as a function of m. SMM results are shown for $\epsilon_0=16$ and $\epsilon_0=8$.

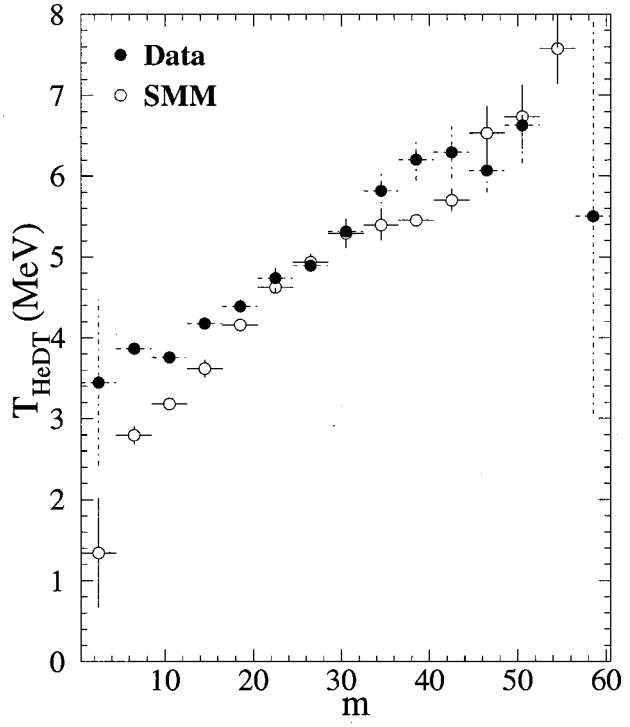

FIG. 12. Dependence of the ^{2}H/^{3}H to ^{4}He/^{3}He(T_{HeDT}) isotopic ratio temperature on *m*.

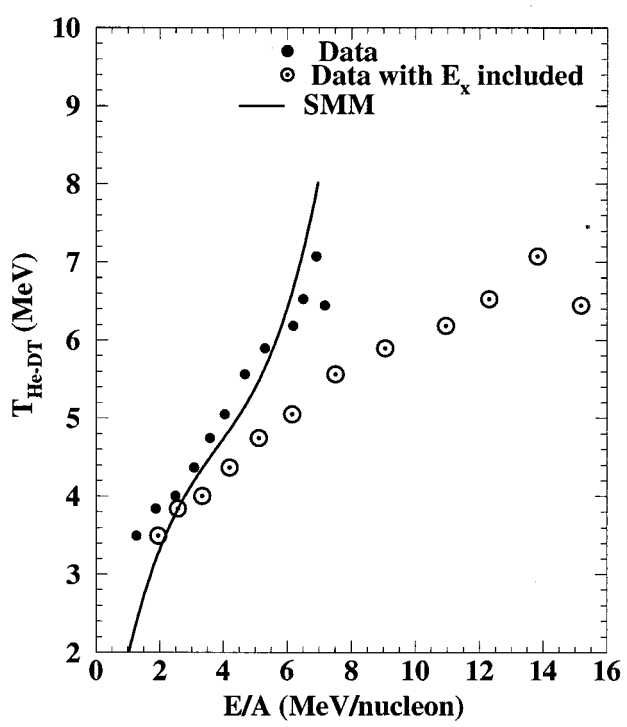

FIG. 13. The caloric curve using the isotopic temperature $T_a = T_{\mathrm{HeDT}}$. Experimental results are shown as a function of both the input energy/nucleon and the total excitation energy/nucleon. The SMM results are for the input excitation energy/nucleon.

double isotopic yield ratios. A value of T_a was also obtained from the ^{6}Li/^{7}Li and ^{3}He/^{4}He yield ratios. Although the two values of T_a are nearly equal, the T_{HeDT} values were found to be more robust [13]. These temperatures are compared with the SMM values in Fig. 12. Excellent agreement in the MF region is observed further confirming the self-consistent nature of data and the predictions of SMM.

It should be noted that the determination of freezeout temperatures obtained by the double isotope yield ratios is subject to correction due to formation of these isotopes in secondary decay. This subject has been investigated by a number of workers [40,51–56]. For the T_{HeDT} thermometer the correction has been reported as ~10% below E_i ~7 MeV/nucleon [13].

B. The caloric curve using isotopic temperatures

The asymptotic caloric curve, which is a plot of fragment isotopic temperatures versus input energy, was first obtained by Pochodzalla *et al.* for 600*A* MeV Au+Au collisions [57]. It was found that the temperature had the essentially constant value of ~5 MeV for excitation energies between 3 and 10 MeV per nucleon, a result that was interpreted as evidence for a first-order phase transition. A similar analysis of the EOS data, in which the excitation energy included the expansion energy, showed that the temperature increased continuously but slowly with E^* over the above range, i.e., from ~4 to ~6 MeV [13]. Having established the presence of nonthermal expansion, we can redetermine our caloric curve and compare it with SMM.

These SMM and EOS caloric curves are compared in Fig. 13, where both SMM isotopic temperatures and experimental isotopic temperatures are plotted versus the experimental input energy E_i per nucleon. The SMM and EOS curves are in close agreement and show a very sharp increase in the temperature *T* over the experimental energy range. Included for comparison is the caloric curve previously obtained with the inclusion of the expansion energy, which shows a much slower variation of *T* with E^*. The determination of a caloric curve in the manner proposed in Ref. [57] has already been shown to be problematic [58–61]. The recent reanalysis by the ALADIN group is in close agreement with our data [62].

It must be noted that experimental caloric curves are actually inadequate measures of the thermodynamic caloric curve, which involves the breakup temperature rather than the isotope ratio temperature. This has been discussed both by Bondorf *et al.* [63] and in a recent publication from our group [17].

C. Critical exponents and related quantities

The EOS Collaboration has analyzed the 1*A* GeV ^{197}Au data in terms of the theory of critical phenomena, according to which MF is viewed as a continuous phase transition. In this section we subject the SMM events to this same analysis and compare the results with those obtained from the data.

1. The critical point multiplicity m_c and the exponent τ

In order to extract the various critical exponents from the data the location of the critical point, which can be characterized by the critical multiplicity, m_c, must be determined. We have used the method presented in Refs. [12,14], in

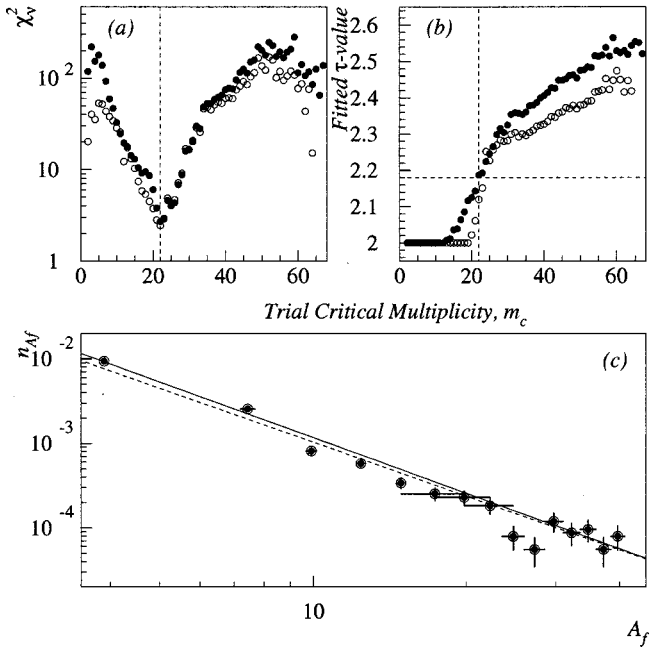

FIG. 14. Determination of τ and m_c from data (Ref. [14]). (a) χ^2_ν values from the power law fit to the fragment mass yield distribution obtained for different m. (b) Values of τ as a function of m. (c) Power law fit to data point $m=m_c$, corresponding to the minimum value of χ^2_ν. The dashed line is a fit to the open points which exclude $A=4$ fragments. The black dot results include the $A=4$ fragments.

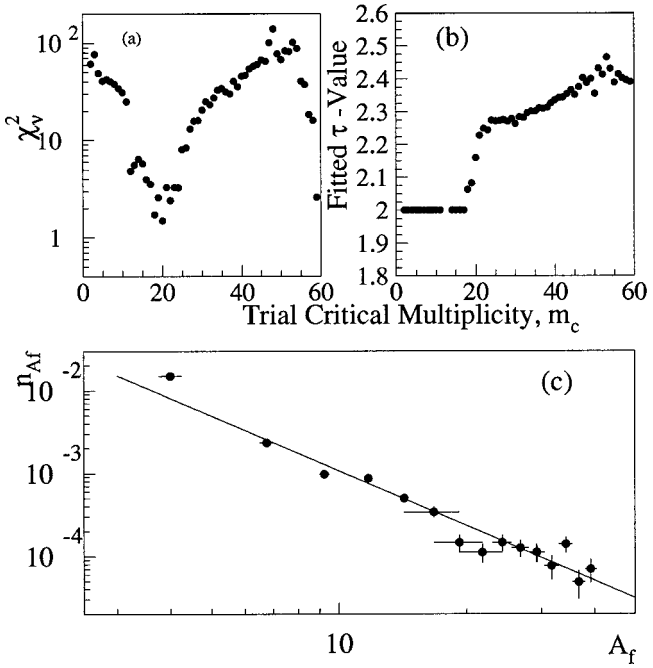

FIG. 15. Determination of τ and m_c from SMM. See Fig. 14 for details.

which m_c, the critical exponents τ, γ and σ, and the scaling function were obtained from the EOS data. We briefly summarize the procedure below. The fragment mass yield distribution, $N_{A_f}(\epsilon)$, where $\epsilon=(m_c-m)/m_c$, is normalized to the mass of the remnant, $A_{\rm rem}(\epsilon)$. The normalized fragment distribution can be written as [64]

$$n_{A_f}(\epsilon)=N_{A_f}(\epsilon)/A_{\rm rem}=q_0A_f^{-\tau}f(z), \tag{7}$$

where $f(z)$ is the scaling function and the scaling variable $z=\epsilon A_f^{\sigma}$. *If we assume that scaling is valid for clusters of all sizes,* then q_0 is a function of only τ,

$$q_0=1/\zeta(\tau-1), \tag{8}$$

where ζ is the Riemann zeta function and $2<\tau<3$ [65,66]. At the critical point $f(z)=1$ and a pure power law is obtained for the fragment mass yield distribution. The power law behavior is modified by the scaling function away from the critical point.

In order to determine m_c and τ one performs power law fits to $n_{A_f}(\epsilon)$ versus A_f for each value of m over a particular range of fragments, e.g., $Z_f=3-16$. The best fit, as determined by the minimum value of χ^2_ν, gives the value of $m=m_c$. The results of this analysis for the EOS data [14] are shown in Fig. 14. The fitting procedure yields a deep minimum in χ^2_ν at $m=m_c=22\pm1$, and thus accurately determines the location of the critical point. The power law fit to the data at this multiplicity is also shown. The value of τ is 2.19 ± 0.02.

The above analysis was also performed for the SMM events for $Z_f=3-16$ and the results are shown in Fig. 15. The dependence of χ^2_ν and τ on m and the quality of the power law fit at m_c are similar to that exhibited by the data. The results are summarized in Table II and are in excellent agreement with the data.

2. Determination of the exponent σ

Once m_c is known, it is possible to determine the value of σ. We have used the percolation procedure where the largest piece $Z_{\rm max}$,$A_{\rm max}$ is removed only on the liquid side [64].

TABLE II. Critical exponents from data and SMM$_{\rm cold}$ (experimental remnants).

Parameter	Data	SMM
m_c	22 ± 1	20 ± 2
τ	2.19 ± 0.02[a]	2.17 ± 0.02
γ	1.4 ± 0.3[a]	1.02 ± 0.23
σ	0.32 ± 0.05[b]	0.63 ± 0.08[c]
	0.54 ± 0.11[b]	

[a]The results differ slightly from those given in Ref. [10] because a larger data set was used in the present analysis [58].
[b]The first value is obtained by including the largest fragment on the "gas" side of m_c. The second value was obtained by adjusting σ for the effect of cooling. The experimental value for the scaling function in Fig. 18(a) was obtained using the second value of σ.
[c]This result is obtained by including the largest fragment on the "gas" side of m_c.

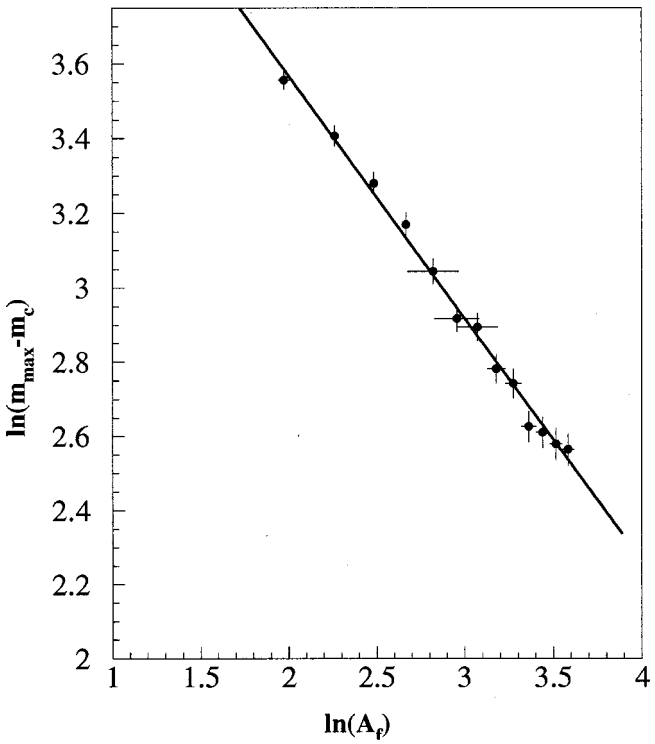

FIG. 16. Determination of σ from SMM. A linear fit of $\ln(m_{\max}-m_c)$ vs $\ln(A_f)$ for $Z=3-15$ fragments gives $\sigma=0.63\pm0.08$.

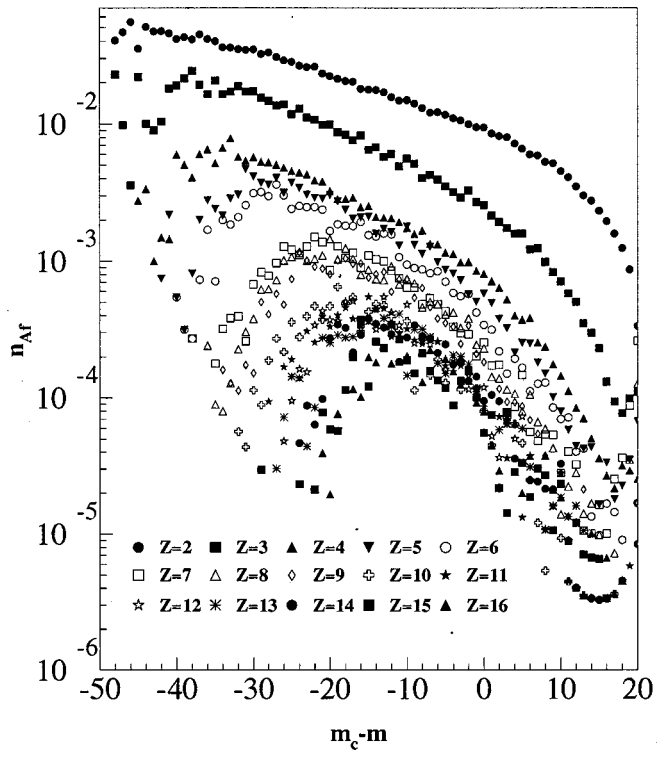

FIG. 17. Unscaled experimental fragment yields for $2\leqslant Z\leqslant 16$.

Since the scaling function must have a single maximum [64], we define $z=z_{\max}=$const as the value of the scaling variable where the maximum for this fragment mass occurs. The previously given relation between z and σ can then be written for this maximum as

$$z_{\max}=\epsilon_{\max}A_f^{\sigma}=\text{const}, \tag{9}$$

where $\epsilon_{\max}=[m_c-m_{\max}(A_f)]/m_c$, with $m_{\max}(A_f)$ being the multiplicity for which the maximum yield of fragments of mass A_f is obtained. Equation (7) leads to a power law, $\epsilon_{\max}\propto A_f^{-\sigma}$, from which σ can be found.

Applying this analysis to SMM, we first determine the values of $m_{\max}(A_f)$. Typical results have been shown in Figs. 8 and 9. Figure 16 shows the power law plot, $\ln(m_{\max}-m_c)$ versus $\ln(A_f)$, from which we obtain $\sigma=0.63\pm0.08$. Applying the same analysis to EOS data, we obtain $\sigma=0.32\pm0.05$, much smaller than the SMM value [67]. The analysis in Sec. V suggests that the σ values in data could be affected by the hot fragment cooling process, and that the σ value adjusted for cooling would be $\sigma=0.54\pm0.11$ (see Table II). This value is used in constructing the scaling function for the EOS data.

3. The scaling function

Knowing the values of m_c, τ, and σ for data and SMM, it is possible to evaluate the scaling function by rewriting Eq. (7) as

$$f(z)=n_{A_f}(\epsilon)/q_0A_f^{-\tau}. \tag{10}$$

The unscaled data is shown in Fig. 17. Scaling $n_{A_f}(\epsilon)$ according to Eq. (10) collapses the multifragmentation data from a broad range of fragments yields onto a narrower band for both data and SMM, as shown in Figs. 18 and 19. Both scaling functions show a comparable scatter of the fragments. By definition, both have a value of unity at the critical point, and both have a maximum of comparable magnitude for virtually the same value of the scaling variable.

4. The exponent γ and moments of the fragment yield distribution

The exponent γ has been determined by means of the γ-matching technique as applied to the second moment, $M_2(\epsilon)$, of the fragment yield distribution [10]. The second moment is defined as

$$M_2(\epsilon)=\Sigma n_{A_f}(\epsilon)A_f^2 \tag{11}$$

and a similar expression may be used if the fragments are characterized by their nuclear charge instead of mass. Again, following the percolation theory procedure, we omit the largest fragment from the summation in Eq. (9) only on the ''liquid'' side of the critical point ($m<m_c$). All fragments are included on the ''gas'' side ($m>m_c$). The exponent γ is obtained from the power law $M_2\propto|\epsilon|^{-\gamma}$ by searching for various multiplicity regions that yield values of γ_{gas} and γ_{liquid} that agree with each other. The value of m_c is again determined in the same fit.

The results for SMM are shown in Fig. 20. The procedure has also been described in Ref. [12] and the results obtained from an analysis of the EOS data are summarized in Table II.

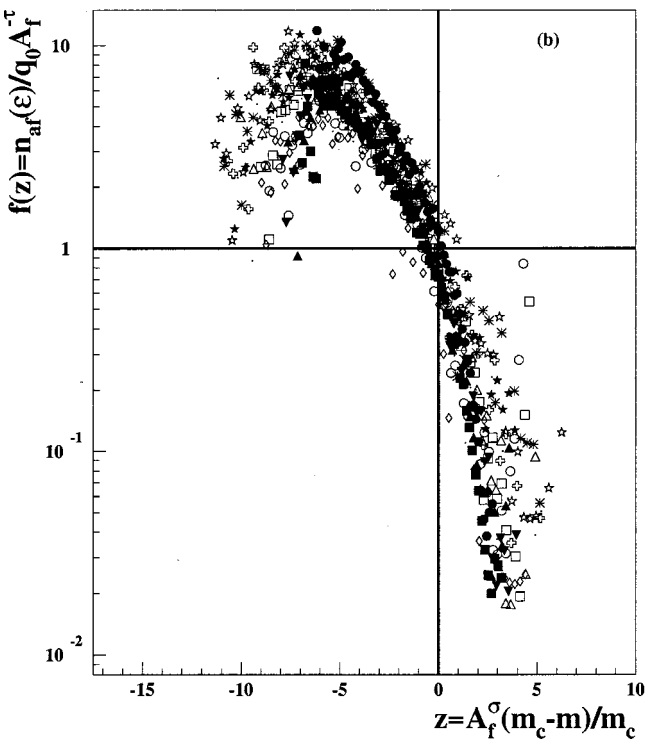

FIG. 18. The scaling functions for data. The intersection of the solid lines marks the critical point.

The same analysis can be applied to the SMM events and the results are also summarized in Table II. The experimental and calculated γ values are consistent within the limits of error.

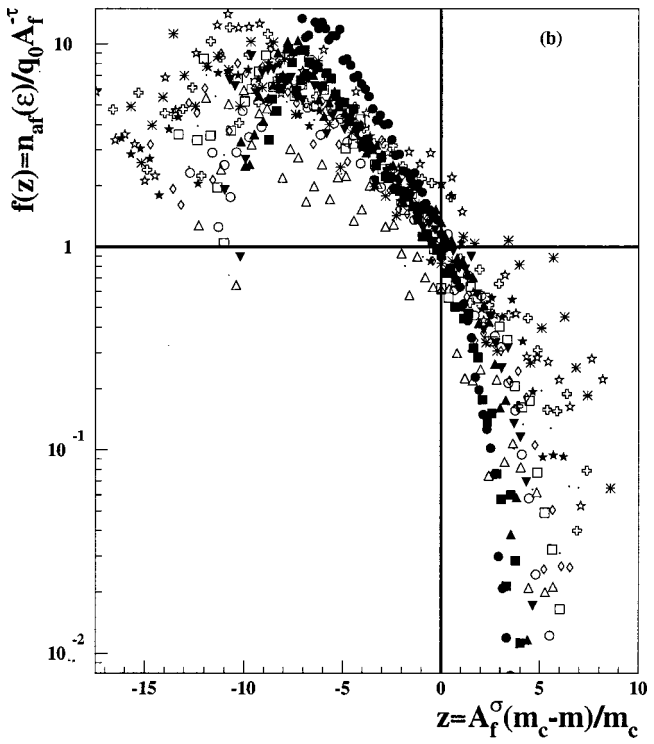

FIG. 19. The scaling functions for SMM. The intersection of the solid lines marks the critical point.

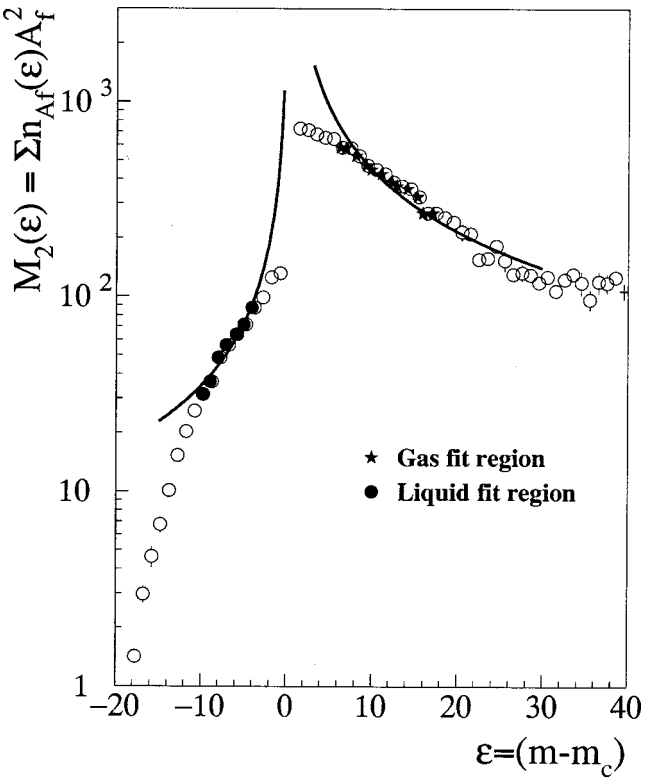

FIG. 20. Second moment of the SMM generated fragment mass yield distribution. The largest fragment has been removed only from the ''liquid'' side ($m<m_c$). All points are from SMM. The solid points from SMM have been used to determine γ. The solid curve is the fit of the power law $M_2=C_{\pm}|\epsilon|^{-\gamma}$.

We have also evaluated several other quantities that have been associated with critical behavior [29,30,68]. They include the fluctuations in the size of the largest fragment and in M_2, the magnitude of the peak in the combination of moments $\gamma_2=M_2M_0/M_1^2$, and the determination of τ from a plot of $\ln M_3$ versus $\ln M_2$. These quantities, too, are in good agreement with experiment.

The fluctuations of the size of the largest fragment and of the moments provide an independent method to locate the critical multiplicity m_c of the MF transition. The first moment M_1 can also indicate how the nucleons are distributed into light particles, IMF's and the largest piece in MF. This distribution can identify the phases present in MF and whether the coexistence of liquid and gas phases occurs in MF. (See Sec. VI.)

V. EFFECTS OF COOLING AND OF THE USE OF A SINGLE REMNANT

The SMM calculations described in the preceding sections give results for deexcited secondary fragments formed from a distribution of remnants. These remnants are grouped according to multiplicity and we have noted that at a given *m* there is a distribution of remnant charges, masses, and excitation energies. An ideal statistical analysis of multifragmentation would involve primary fragments formed from the breakup of a unique remnant (*A*, *Z*) as a function of remnant

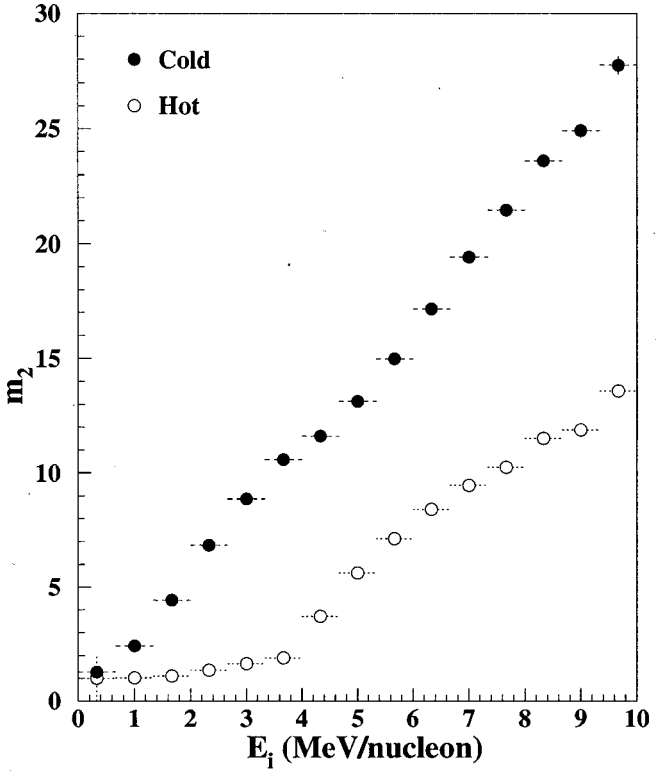

FIG. 21. Second stage multiplicity m_2 for SMM_{cold} and SMM_{hot}.

excitation energy or temperature. In this section we use SMM to examine the extent to which the departures from this ideal situation affect the values of the critical exponents and related fragment properties. We introduce the terms SMM_{hot} and SMM_{cold} to designate results obtained from SMM for primary fragments and deexcited fragments, respectively.

A. Hot and cold SMM fragment yields

The most direct view of the effect of deexcitation is provided by a comparison of the SMM_{hot} and SMM_{cold} fragment yield distributions. For simplicity, we evaluate these distributions for the decay of a single remnant as a function of E_i. We have chosen the remnant formed in the Au on C interaction corresponding to the critical multiplicity in the data, $A=160$, $Z=64$, and evaluated its breakup for a range of E_i values. At a given m the total rms width of the remnant distribution is $\sim$5–7 %. In SMM the average Z/A ratio of the hot ''prefragments'' is the same as the remnant Z/A ratio, i.e., no particles or energy leaves the remnant system during the $\sim$100 fm/c time frame for MF.

The increase in the charged particle multiplicity m_2 from SMM_{hot} to SMM_{cold} is shown in Fig. 21. This figure shows that cooling is important. Typical results for fragments with $Z>3$ are shown in Figs. 22 and 23. The fragment multiplicities for SMM_{hot} and SMM_{cold} are in close agreement up to $E_i \simeq 7$ MeV/nucleon. However, at higher excitation energies the primary fragment yields are significantly larger than those of the corresponding cold fragments. At these high E_i,

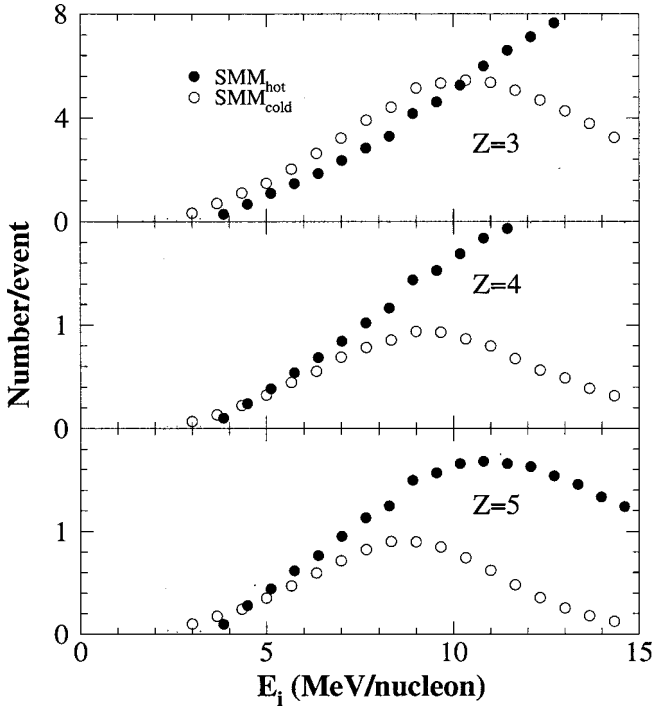

FIG. 22. Multiplicity of $Z=3,4,5$ fragments as a function of input energy for SMM_{hot} and SMM_{cold} in MF of $A=160$, $Z=64$.

fragments undergo substantial secondary decay, which according to SMM, occurs by evaporation for fragments with $A>16$. For $A<16$, secondary decay occurs by Fermi breakup. These mechanisms tend to form the lightest particles and thereby reduce the yields of fragments with Z

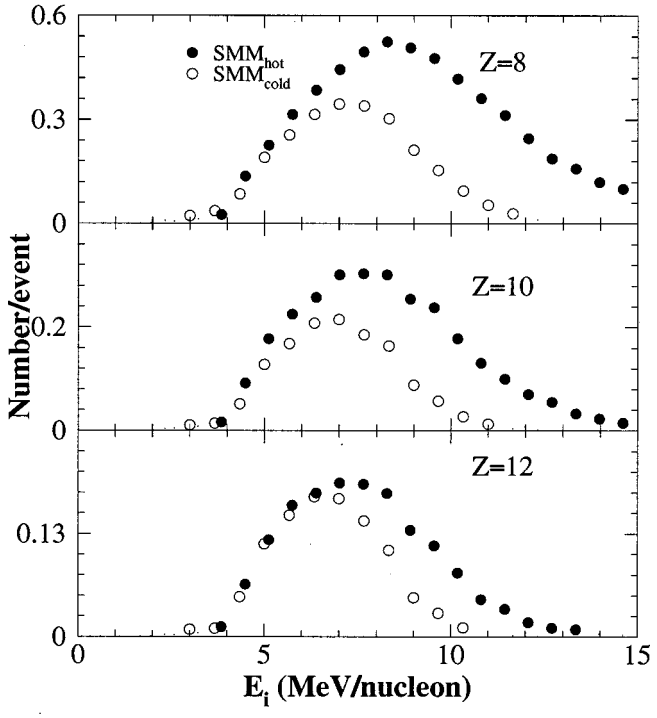

FIG. 23. Multiplicity of $Z=8,10,12$ fragments as a function of input energy for SMM_{hot} and SMM_{cold} in MF of $A=160$, $Z=64$.

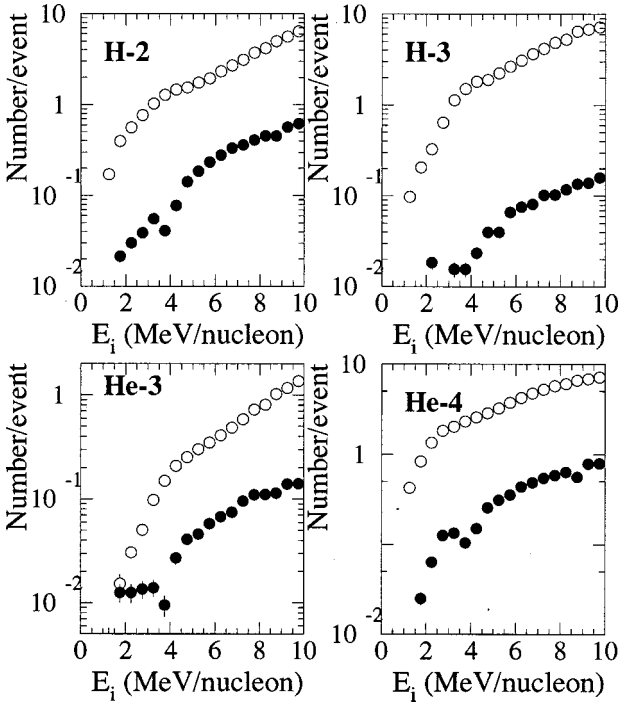

FIG. 24. Multiplicity of $Z=1$ and 2 particles as a function of input energy for SMM_{hot} (solid circles) and SMM_{cold} (open circles) in MF of $A=160$, $Z=64$. Note that most of these particles are produced in the cooling process.

$\geqslant 3$. We emphasize the fact that the net effect of these secondary processes on the fragment distributions is rather small below 7 MeV/nucleon, the energy range where most of the MF occurs. The critical point corresponds to a much lower excitation energy, $E_i \sim 4.3$ MeV/nucleon [13], and therefore quantities determined at these low energies should be nearly unaffected.

Figure 24 shows the results for $Z=1$ and $Z=2$ particles. Contrary to the results shown in Figs. 22 and 23, most of these particles are formed in the cooling step. Averaging over the excitation energy range important for MF, 3–7 MeV/nucleon, we find that the lightest hot fragments have a higher internal energy per nucleon than the heavier hot fragments, ~ 4 MeV/nucleon versus ~ 3 MeV/nucleon. Consequently the main source of these particles is the Fermi breakup of the lighter fragments.

B. Effect of cooling on critical exponents and related quantities

The analysis described in Sec. IV C has been applied to the products of SMM_{hot}, using the experimental remnants as input. The resulting values of the various exponents are tabulated in Table III. The calculated value of τ for hot fragments is $\sim 6\%$ smaller than that for cold fragments while that of γ is $\sim 11\%$ smaller. In contrast, the determination of the exponent σ differs significantly for the two distributions, with the SMM_{hot} value being $\sim 40\%$ larger than that from SMM_{cold}. The large difference in σ values is understandable given that σ is determined in part by the multiplicities for which the various fragments attain their highest yields. As shown in Figs. 8 and 9, the yields of the lighter fragments peak at large values of m, corresponding to E_i values of 7 MeV/nucleon and higher. It is precisely at these energies that secondary decay reduces the yield of these fragments and thereby leads to a smaller σ.

TABLE III. Critical exponents from SMM_{hot} and SMM_{cold}.

	Experimental remnant distribution		Single remnant $A=160$, $Z=64$	
Parameter	SMM_{cold}	SMM_{hot}	SMM_{cold}	SMM_{hot}
m_c	12 ± 2	5 ± 2	12 ± 2	5 ± 2
τ	2.17 ± 0.02	2.05 ± 0.02	2.07 ± 0.01	2.03 ± 0.01
γ	1.02 ± 0.23	0.91 ± 0.20	1.10 ± 0.20	0.97 ± 0.15
σ	0.62 ± 0.08	1.04 ± 0.11	0.69 ± 0.02	1.00 ± 0.07

In a recent publication Mastinu *et al.* [45] used the Copenhagen model to examine the effect of secondary fragment decay in the MF of ^{197}Au. In particular, they compared the shape of the second moment, M_2, of the fragment charge distribution for SMM_{hot} and SMM_{cold}. They found that the shape of the M_2 distribution in the vicinity of its peak is unaffected by secondary decay when plotted against E^* whereas there is a change in shape when M_2 is plotted against m.

On this basis they concluded that secondary decay affects the values of exponents such as γ, which is obtained from M_2, when charged particle multiplicity is used as the control parameter. Unfortunately, they did not calculate the magnitude of this effect. We have already evaluated the effect on γ of secondary decay and, as shown in Table III find that it is a relatively small 10% correction. We note in passing that the M_2 plot shown by Mastinu *et al.* [45] is not appropriate for the extraction of γ because the largest fragment has been removed from *both* the liquid and gas sides instead of only on the liquid side, as was done in Fig. 20. Furthermore, they did not turn off the fission channel in their SMM calculation and the contribution of this mechanism disproportionately affects the analysis.

C. Critical exponents from the multifragmentation of a single remnant for SMM_{hot}

The analysis described in Sec. IV C is applied to the breakup of a single remnant, using the *input energy* as the control parameter. We use the critical remnant $A=160$, $Z=64$ as the system size for SMM. Figure 25 shows the SMM_{hot} results for the determination of the critical point by means of the one-parameter power law fit to the fragment mass yield distribution.

Again, there is a deep minimum in χ_v^2 which determines the location of the critical point. This should be compared with the same results for SMM_{cold} using the experimental remnant distribution and m as the control parameter (Fig. 15).

The value of τ obtained from the fit in Fig. 25 is given in Table III. Also included are the values of the other exponents. A comparison with the corresponding exponents ob-

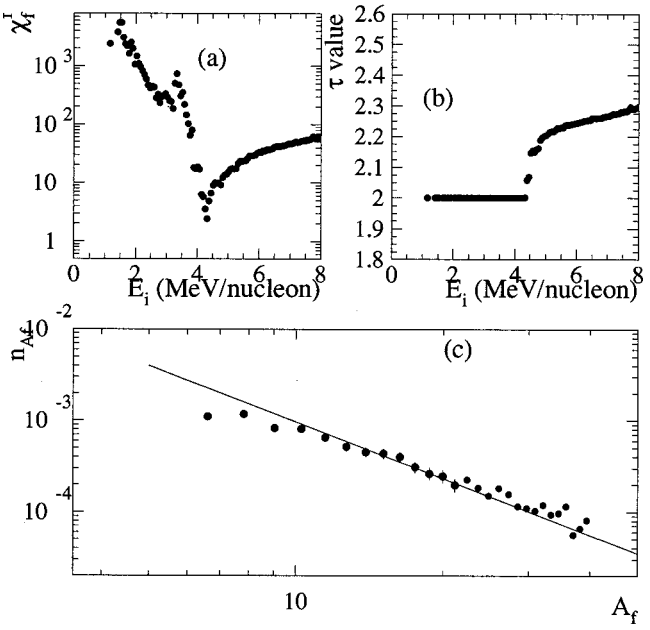

FIG. 25. Determination of τ and E_c in the MF of $A=160$, $Z=64$ for SMM_{hot}. The panels have the same meaning as in Fig. 14 except that E_i replaces m as the control parameter.

tained for SMM_{cold} for the experimental remnant distribution indicates that the difference in τ and γ values is less than 10%. Thus the combined effect of secondary decay, the remnant distribution for a given m, and the use of multiplicity as the control parameter have only a minor effect on the values of the τ and γ exponents. However, the exponent σ for SMM_{hot} is much larger than the corresponding value of SMM_{cold} just as was the case for the experimental remnant distribution. Again, this difference reflects the effect of cooling. We note here that the use of a single remnant and excitation energy as the control parameter, which is most readily seen in a comparison of the two SMM_{hot} columns, has essentially no effect on the critical exponents.

Figure 26 shows the unscaled SMM_{hot} fragments for $A=5$ to 30 for the single remnant system. Figure 27 shows the scaling function obtained from these data and the resulting scaling collapse of the data into a very narrow band. This scaling function should be compared with the scaling function from SMM_{cold} (Fig. 19). The more extensive scatter in Fig. 19 can be attributed in comparable measure to the effects of fragment cooling and to the presence of the remnant distribution, using multiplicity as the control parameter. This indicates that the scatter seen in the experimental data at the ends of the scaling curves, Fig. 18, may also be due to these effects.

VI. NATURE OF THE PHASE TRANSITION IN SMM

We have shown that SMM can reproduce the various features of the EOS data, including the values of most of the critical exponents, critical multiplicity, and critical scaling. If SMM did not predict the occurrence of a continuous phase transition then the exponents would merely constitute a particular parametrization of the data and would have no ulterior

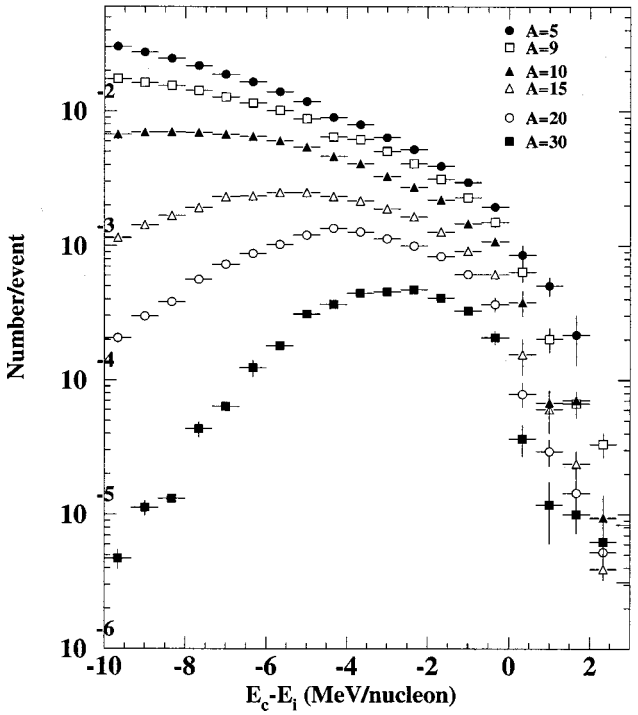

FIG. 26. Unscaled yield of fragments/event from SMM_{hot} for $A=5-30$ as a function of E_c-E_i.

significance. It is therefore important to determine if SMM predicts such a thermal phase transition.

We follow the approach of Gross [69] and Hüller [70], who show that the nature of the transition can be determined

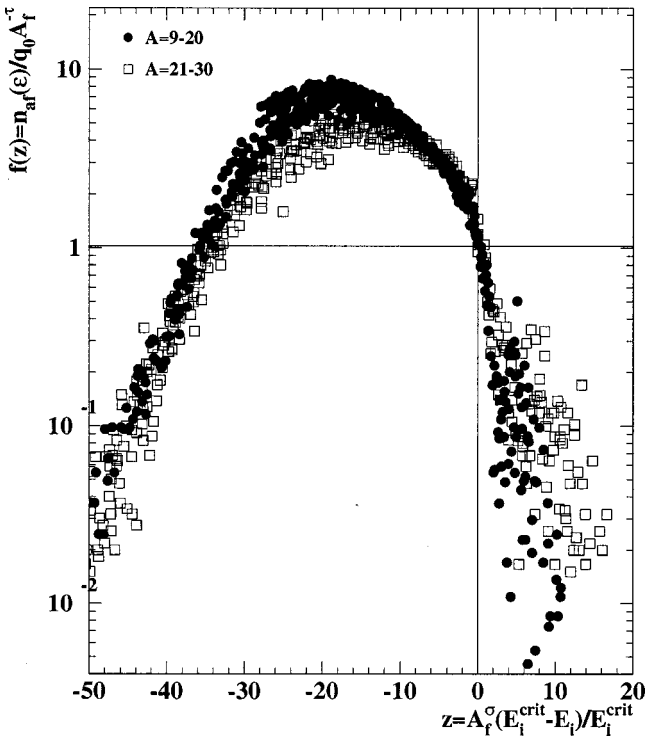

FIG. 27. Scaling function obtained from SMM_{hot} for MF of $A=160$, $Z=64$.

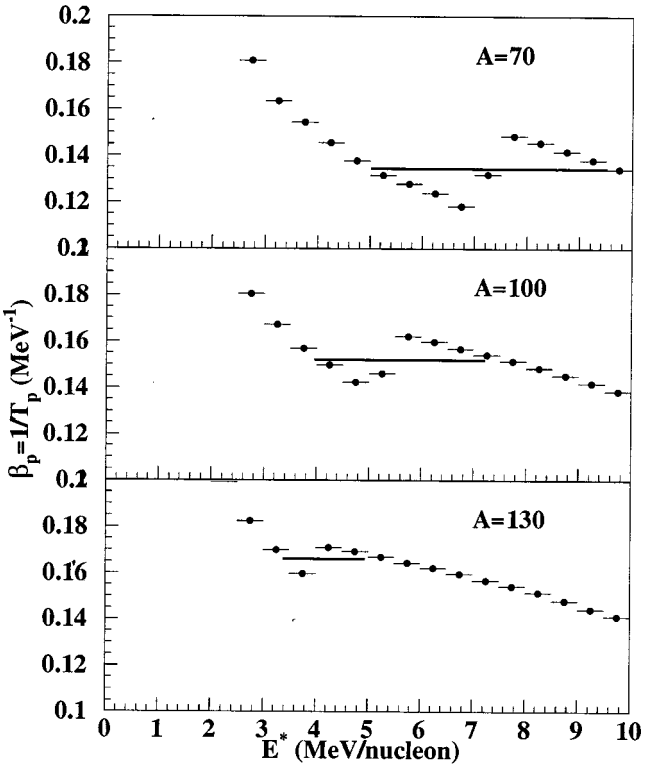

FIG. 28. Dependence of β_p on the input energy for $A=70$, 100 and 130. The lines are drawn for equal area and show the ''Maxwell construction.''

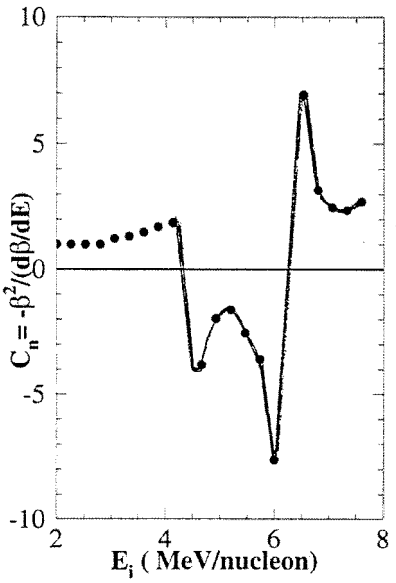

FIG. 29. System specific heat per particle for $A=100$. The solid curve is to guide the eye.

by means of the microcanonical equation of state, using a plot of the reciprocal partition temperature $\beta_p = 1/T_p$ versus E_i. We assume T_p is the best estimate of the average value of the fluctuating event-by-event SMM microcanonical temperature. A first order transition is identified by backbending in the β_p vs E_i curve and hence has a region of negative system specific heat, $C_n = -\beta_p^2/(d\beta_p/dE_i)$. A continuous phase transition will not exhibit backbending and will have a positive system specific heat that peaks at the critical energy.

Recall that for infinite neutral nuclear matter a critical phase transition is expected at a temperature ~15–18 MeV [46]. At lower temperatures, infinite neutral nuclear matter would exhibit a first order liquid-gas phase transition with possible coexistence of constant density phases. SMM, however, describes the transition of a highly excited *finite charged* nuclear drop into a number of hot intermediate mass fragments followed by a deexcitation process. The cold state liquid and gas consists of smaller droplets and nucleons emitted in the cooling process. In the hot stage, the so-called prefragments are produced in thermodynamic equilibrium where the volume, surface, Coulomb, symmetry and translational terms determine the fragment yields [32].

To investigate the interplay of these energy terms we study SMM$_{\rm hot}$ as a function of the remnant mass and charge [71]. Figure 28 shows β_p versus E_i curves for $A=70$, $Z=30$; $A=100$, $Z=40$; and $A=130$, $Z=53$. A characteristic backbending is observed for these systems. Following the microcanonical prescription, we make the ''Maxwell construction'' [69], which determines the average transition temperature and the magnitude of the transition energy or effective latent heat. For $A=100$ we obtain a transition energy of 3.2 MeV/nucleon as given by the width of the backbend region. Figure 29 shows that the system specific heat for $A=100$ is negative indicating the possibility of a first order phase transition. We have computed the effect of the variable volume on the system specific heat and found that it is a very small fraction of the total. The translational energy contribution is also very small. Thus C_n describes the change in the internal energy of the MF system. The transition energy plays the role of an effective latent heat for MF. SMM$_{\rm hot}$ indicates that the effective latent heat is reduced for heavier remnants. For the $A=70$, 100, and 130 systems, there is a progressive decrease in the transition energy as shown in Fig. 30. A linear extrapolation suggests that the transition energy as an effective latent heat could vanish for $A>170$. We can gain further insight about these transitions by studying the distributions of light particles and fragments prior to the deexcitation or cooling process. For $A=100$ the first moment of the hot mass distribution as a function of the input energy is shown in Fig. 31. For $E_i=8$ MeV/nucleon only ~5 out of 100 nucleons are not part of the $A>4$ droplet distribution. Thus hot SMM describes a transition where a large droplet is multifragmented into smaller droplets. The subsequent deexcitation processes are responsible for most of the light particles with $A<5$ seen in the asymptotic mass distributions.

In this SMM model backbending can be a relatively large effect. The extra surface energy required for the MF transition cools the system and the temperature falls. For a larger system the fractional change in the surface to volume ratio due to MF is reduced and the backbending is smaller. In SMM the total Coulomb energy is reduced by the factor $1-1/(1+\kappa)^{1/3} \sim 0.3$ due to expansion prior to clusterization. Since the total energy is measured with respect to the ground state of the remnant system A, Z at normal density, this in-

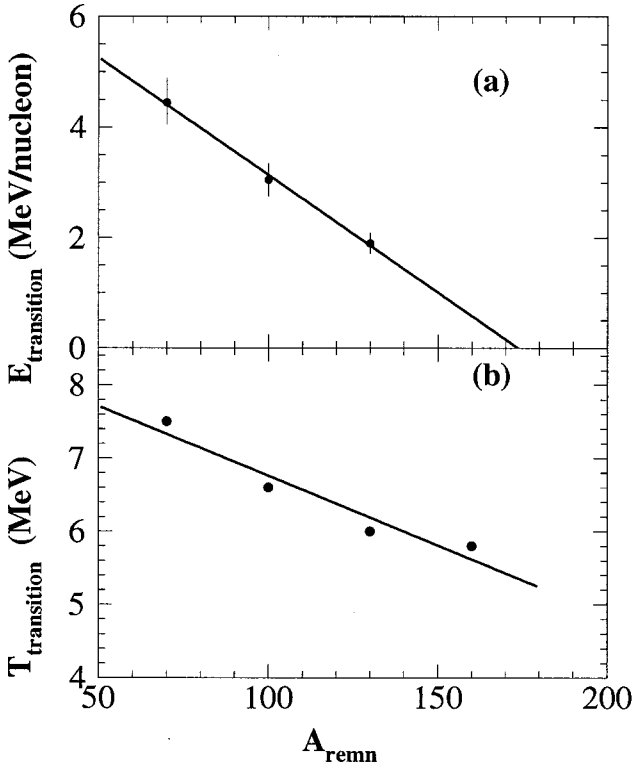

FIG. 30. (a) MF transition energy, the effective latent heat, for $A=70$, $A=100$, and $A=130$. (b) Average, i.e., Maxwell construction, transition temperature for $A=70$, $A=100$, $A=130$, and $A=160$.

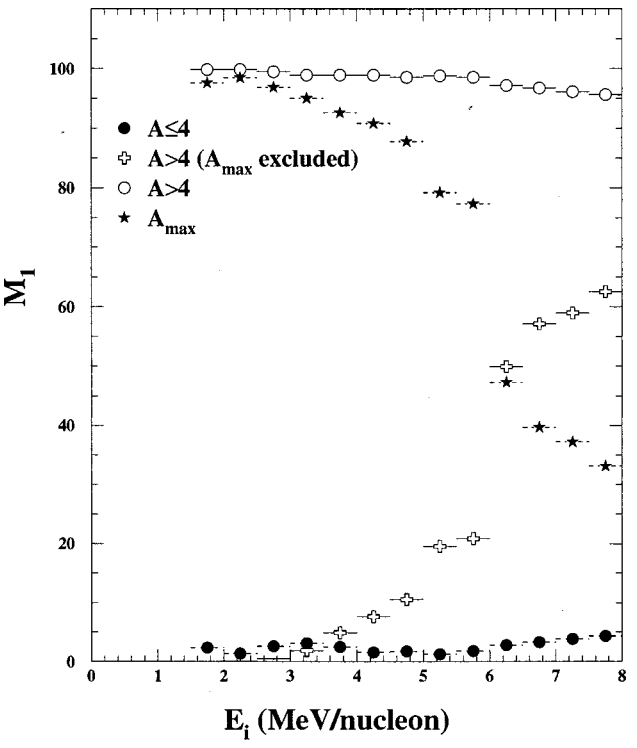

FIG. 31. First moment of the SMM_{hot} mass distribution for $A=100$.

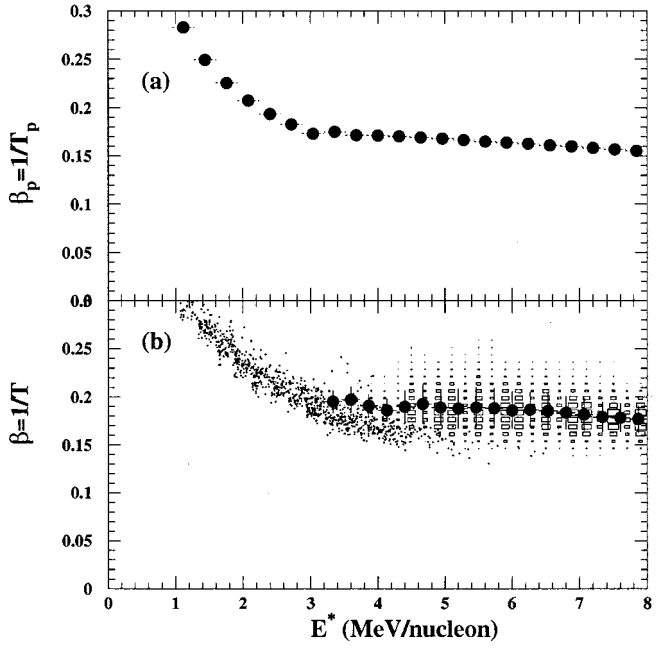

FIG. 32. (a) Dependence of β_p on the input energy E_i for $A=160$. (b) Event to event fluctuations of β versus the input energy for $A=160$. The dot scatter points identify compound nucleus events; the box scatter points identify MF events. The solid block dots are the average β values for MF events.

troduces a Z dependence into the β_p versus E_i equation of state.

Figure 30(b) shows the average transition temperature, which decreases as the remnant mass and charge increases. This decrease clearly reflects the increase in Coulomb energy for the heavier remnants [72]. In contrast, for a liquid-gas phase transition in *finite neutral matter* we would expect the transition temperature to increase with the system size, because the binding energy per nucleon increases. For a larger charged nuclear remnant, the transition energy will vanish if enough Coulomb energy is converted to heat energy in the expansion of the remnant prior to the MF transition.

For the remnant mass $A=160$ the reciprocal partition temperature β_p is plotted versus E_i in Fig. 32(a) and the fluctuating event-by-event reciprocal microcanonical temperatures β_p, are shown in Fig. 32(b). The area under the β_p vs E_i curve is the system entropy. In Fig. 33(a), we expand the β_p vs E_i plot. The system specific heat per particle is computed by taking differences between adjacent points. C_n is shown in Fig. 33(b). The specific heat is positive and peaks near the critical energy, indicating a continuous phase transition. Hüller characterizes such behavior as a continuous phase transition with an anomalous specific heat [70].

A method to determine the order of the phase transition based on canonical kinetic energy fluctuations has recently been proposed [73–75]. To test the conclusions based on the SMM_{hot} microcanonical equation of state, we have done this type of analysis on the Au on C data. For a single remnant system size A, Z this analysis compares the canonical spe-

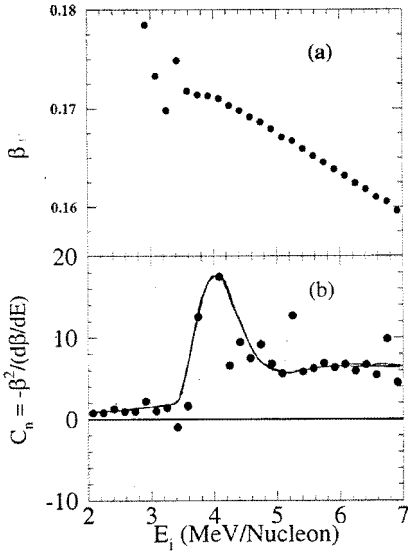

FIG. 33. (a) Expanded β_p vs E_i curve. (b) System specific heat per particle for $A=160$.

cific heat C_1 with the thermally scaled kinetic energy fluctuations $(E^2-\langle E\rangle^2)/T^2$.

Following the prescription used on the 35 MeV/nucleon Au on Au data we find that the energy fluctuations from the Au on C data are dramatically reduced when a $\Delta A/A \leqslant 0.03$ remnant mass cut is made, which assures that we have a single system size, the necessary constraint for the fluctuation analysis. Thus for the Au on C data, we find that $C_1 > (E^2-\langle E\rangle^2)/T^2$ in the whole MF region. The value of C_1 still remains positive even for a larger remnant mass cut, e.g., $\Delta A/A \sim 10\%$. This result argues for a continuous phase transition. A report of this work is in preparation.

Very recently (since the submission of the present article), theoretical analyses of the nature of MF phase transition and its effect on the caloric curve have been published [76,77], indicating the occurrence of a first order phase transition. Both of these calculations neglect the Coulomb interaction, which has been shown to play an important role in MF [72]. It is obvious that there will be a first order phase transition in the absence of Coulomb energy.

It has been suggested on the basis of a caloric curve using the SMM partition temperature versus an experimentally determined input energy, that MF of gold is a first order liquid-gas phase transition [57]. This curve, computed for comparison with the ALADIN data showed that the temperature first increases with excitation energy, then remains nearly constant at 5–6 MeV as E_i increases between 3 and 10 MeV/nucleon, and then again increases. The first regime has been interpreted as the liquid phase, i.e., the compound nucleus, the second as the MF coexistence phase, and the third as the gas phase, consisting of a mixture of nucleons and a few of the lightest fragments [63]. This viewpoint can be probed by examining the first moment of the *hot fragment* yield distribution for a heavy remnant. Figure 34(b) shows a plot of the dependence on E_i of the first moment of the hot fragment yield distribution for the experimental remnant distribution.

The figure shows that even for $E_i \sim 8$ MeV/nucleon, well above the MF transition, only about 8% of the remnant mass ends up in particles with $A \leqslant 4$ and that the other 92% are in intermediate mass fragments with $A>4$. This argues against the coexistence of the constant density liquid and gas phases in SMM. For the experimental remnant distribution, we compare the first moment M_1, for $\mathrm{SMM_{hot}}$ Fig. 34(b) with M_1 for $\mathrm{SMM_{cold}}$ as shown in Fig. 34(a). The cooling of the hot fragments which carry the multifragmentation signal produces a large number of final state nucleons and light composites in agreement with the data. The IMF's survive the cooling process and identify the MF transition. This is due in part to the low ~4.3 MeV/nucleon critical energy for MF. For an $A=70$, $Z=30$ remnant, the predicted center of the backbend region energy is ~7.5 MeV/nucleon. Here, the hot fragments will have to emit a significantly higher fraction of their fragment mass in the cooling process and the MF signal could be severely attenuated. Thus the Coulomb energy, which lowers the MF threshold and reduces the effective latent heat, plays a central role in MF. Here the vanishing transition energy reflects the changes in the surface, volume, and Coulomb energies associated with MF rather than the traditional latent heat in a liquid-gas phase transition, which primarily involves the transfer of individual nucleons from the liquid to the gas, where both phases are at constant density ρ_{liquid} and ρ_{gas}.

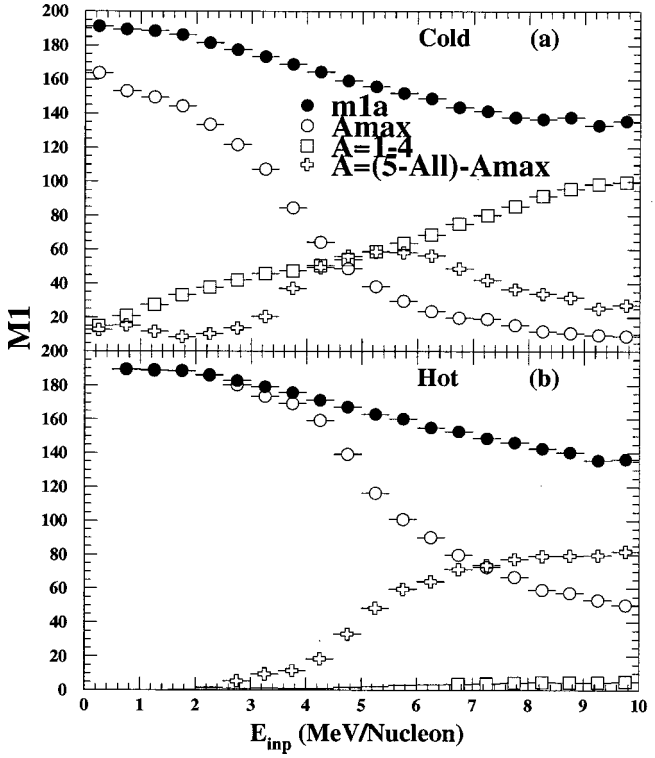

FIG. 34. (a) First moment of the mass distribution from $\mathrm{SMM_{cold}}$ for the experimental remnant distribution. (b) First moment of the mass distribution from $\mathrm{SMM_{hot}}$. The cooling mechanism is nucleon and $A \leqslant 4$ composite particle emission.

VII. SUMMARY AND CONCLUSIONS

We have compared the EOS multifragmentation results for 1*A* GeV Au on C with the SMM model, where the vol-

ume parametrization is determined by experiment. We have found that the standard SMM parameters produced excellent agreement. The input to SMM consisted of the Z, A, and E_i of the individual remnants produced in some 32 000 fully reconstructed events. Thus, in contrast to earlier experiments which have been compared with SMM, the A,Z,E_i event-by-event input data were obtained from experiment rather than by using SMM to constrain average input conditions, or by the use of a theoretical first stage transport model.

We find that SMM is in very good agreement with the observed fragment charge yield distribution, fragment multiplicity distributions, total charged particle multiplicity, isotope ratio temperatures and caloric curve. This agreement is obtained when the expansion energy is subtracted from the experimentally determined excitation energy of the remnant. The agreement provides further confirmation that multifragmentation can be described as an equilibrium process.

SMM also predicts a power law for the fragment mass yield distribution at essentially the same multiplicity or excitation energy as is observed in the data. Other features characteristic of a continuous phase transition, such as the scaling function, are also reproduced. The critical exponents τ, γ, and σ were obtained from SMM for comparison with the experimental values. The agreement is excellent for τ, which is based on results obtained just at the critical point, fair for γ which is based on results obtained above and below the critical point, and poor for σ, which is based on results well above the critical point.

The effect of cooling of the primary hot fragments produced by SMM has been evaluated. The primary hot fragment yield distributions for $Z \geqslant 3$ are only minimally affected by the cooling process below $E_i = 7$ MeV/nucleon. The SMM σ values are substantially affected by cooling, while τ and γ are unaffected by cooling. The scaling function obtained for $\mathrm{SMM_{hot}}$ is fully collapsed into a very narrow band. In contrast to fragments with $Z \geqslant 3$, the yield of particles with $Z \leqslant 2$ is substantially increased by cooling, primarily as a result of the Fermi breakup of light fragments.

We have also performed SMM calculations in which the experimental remnant distribution has been replaced by a single average remnant. The results are virtually unchanged indicating that the mixing of different remnants in the experimental data does not affect the results. We have used both multiplicity and excitation energy as the control parameter in the determination of critical exponents and related quantities and find no difference.

The nature of the phase transition predicted by SMM has been examined using the microcanonical equation of state. For lighter remnants we find evidence of backbending in the caloric curve and a negative system specific heat, which are the signatures of a first-order phase transition. We estimate the transition energy by means of a Maxwell construction. The transition energy decreases with increasing remnant mass and charge and may extrapolate to zero just above $A = 160$, which might suggest a continuous phase transition in the breakup of this remnant. Here the positive system specific heat peaks at the same E_i value for which both data and SMM fragment mass yield distributions obey a power law. For both the first order and continuous phase transition cases, $\mathrm{SMM_{hot}}$ indicates that the multifragmentation final state consists of droplets with $A > 4$ and that particles having $A \leqslant 4$ account for only $\sim$8% of the mass in the MF region.

The SMM results agree with the theoretical expectations for a small ($\sim$150 constituents) isolated system [33,69,78]. The most probable equilibrium state of a highly excited small isolated system with short range interactions is an inhomogeneous state. The addition of the long range Coulomb force lowers the MF transition temperature significantly for heavier remnants and can influence the order of the thermal phase transition. Both the microcanonical equation of state and thermally scaled kinetic energy fluctuation arguments favor a continuous phase transition.

ACKNOWLEDGMENTS

We thank Dr. A. S. Botvina for giving us the SMM code and for valuable discussions concerning its use. This work was supported by the U.S. Department of Energy under Contract Nos. DE-FG02-88, ER 40412C.

[1] J. Hübele *et al.*, Z. Phys. A **340**, 263 (1991).
[2] S. C. Jeong *et al.*, Phys. Rev. Lett. **72**, 3468 (1994).
[3] P. Desesquelles *et al.*, Phys. Rev. C **48**, 1828 (1993).
[4] J. C. Steckmeyer *et al.*, Phys. Rev. Lett. **76**, 4895 (1996).
[5] K. B. Morley *et al.*, Phys. Rev. C **54**, 737 (1996).
[6] G. F. Peaslee *et al.*, Phys. Rev. C **49**, R2271 (1994).
[7] W. G. Lynch, Annu. Rev. Nucl. Part. Sci. **37**, 493 (1987).
[8] L. G. Moretto and G. J. Wozniak, Annu. Rev. Nucl. Part. Sci. **43**, 379 (1993).
[9] G. Peilert, H. Stöcker, and W. Greiner, Rep. Prog. Phys. **57**, 533 (1994).
[10] M. L. Gilkes *et al.*, Phys. Rev. Lett. **73**, 1590 (1994).
[11] J. A. Hauger *et al.*, Phys. Rev. Lett. **77**, 235 (1996).
[12] J. B. Elliott *et al.*, Phys. Lett. B **381**, 35 (1996).
[13] J. A. Hauger *et al.*, Phys. Rev. C **57**, 764 (1998).
[14] J. B. Elliott *et al.*, Phys. Lett. B **418**, 34 (1998).
[15] J. Lauret *et al.*, Phys. Rev. C **57**, R1051 (1998).
[16] B. K. Srivastava *et al.*, Phys. Rev. C **60**, 064606 (1999).
[17] J. A. Hauger *et al.*, Phys. Rev. C **62**, 024616 (2000).
[18] J. B. Elliott *et al.*, Phys. Rev. C **49**, 3185 (1994).
[19] J. B. Elliott *et al.*, Phys. Rev. C **55**, 1319 (1997).
[20] J. A. Gaidos *et al.*, Phys. Rev. Lett. **42**, 82 (1979).
[21] J. E. Finn *et al.*, Phys. Rev. Lett. **49**, 1321 (1982).
[22] R. W. Minich *et al.*, Phys. Lett. **118B**, 458 (1982).
[23] A. S. Hirsch *et al.*, Phys. Rev. C **29**, 508 (1984).
[24] T. C. Sangster *et al.*, Phys. Lett. B **188**, 29 (1987).
[25] M. Mahi *et al.*, Phys. Rev. Lett. **60**, 1936 (1988).
[26] N. T. Porile *et al.*, Phys. Rev. C **39**, 1914 (1989).
[27] M. E. Fisher, Physics (N.Y.) **3**, 255 (1967).
[28] C. J. Waddington and P. S. Freier, Phys. Rev. C **31**, 888 (1985).

[29] X. Campi, J. Phys. A **19**, L917 (1986).
[30] X. Campi, Phys. Lett. B **206**, 351 (1988).
[31] A. Schüttauf *et al.*, Nucl. Phys. **A607**, 457 (1996).
[32] J. Bondorf *et al.*, Phys. Lett. **150B**, 57 (1985); Nucl. Phys. **A443**, 321 (1985); **A444**, 460 (1985); Phys. Rep. **257**, 133 (1995).
[33] D. H. E. Gross, Rep. Prog. Phys. **53**, 605 (1990).
[34] J. Hübele *et al.*, Phys. Rev. C **46**, R1577 (1992).
[35] H. W. Barz *et al.*, Nucl. Phys. **A561**, 466 (1993).
[36] P. Kreutz *et al.*, Nucl. Phys. **A556**, 672 (1993).
[37] A. Botvina *et al.*, Nucl. Phys. **A584**, 737 (1995).
[38] P. Desquelles *et al.*, Nucl. Phys. **A604**, 183 (1996).
[39] M. D'Agostino *et al.*, Phys. Lett. B **371**, 175 (1996).
[40] H. Xi *et al.*, Z. Phys. A **359**, 397 (1997).
[41] C. Williams *et al.*, Phys. Rev. C **55**, R2132 (1997).
[42] X. Campi, H. Krivine, and E. Plagnol, Phys. Rev. C **50**, R2680 (1994).
[43] W. Bauer and A. Botvina, Phys. Rev. C **52**, R1760 (1995).
[44] W. Bauer and W. A. Friedman, Phys. Rev. Lett. **75**, 767 (1995).
[45] P. F. Mastinu *et al.*, Phys. Rev. C **57**, 831 (1998).
[46] D. G. Ravenhall, C. J. Pethick, and J. M. Lattimer, Nucl. Phys. **A407**, 572 (1983).
[47] S. Fritz, Ph.D. thesis, University of Frankfurt, 1997.
[48] P. Danielewicz, Phys. Rev. C **51**, 716 (1995).
[49] P. G. Warren, Ph.D. thesis, Purdue University, 1996.
[50] S. Albergo *et al.*, Nuovo Cimento A **89**, 1 (1985).
[51] Y.-G. Ma *et al.*, Phys. Lett. B **390**, 41 (1997).
[52] M. J. Huang *et al.*, Phys. Rev. Lett. **78**, 1648 (1997).
[53] M. B. Tsang *et al.*, Phys. Rev. Lett. **78**, 3836 (1997).
[54] H. Xi *et al.*, Phys. Lett. B **431**, 8 (1998).
[55] H. F. Xi *et al.*, Phys. Rev. C **59**, 1567 (1999).
[56] H. Xi *et al.*, Phys. Rev. C **58**, R2636 (1998).
[57] J. Pochodzalla *et al.*, Phys. Rev. Lett. **75**, 1040 (1995).
[58] J. B. Natowitz *et al.*, Phys. Rev. C **52**, R2322 (1995).
[59] X. Campi, H. Krivine, and E. Plagnol, Phys. Lett. B **385**, 1 (1996).
[60] L. G. Moretto *et al.*, Phys. Rev. Lett. **76**, 2822 (1996).
[61] V. Serfling *et al.*, Phys. Rev. Lett. **80**, 3928 (1998).
[62] W. F. J. Muller, *Proceedings of the International Workshop XXVII on Gross Properties of Nuclei and Nuclear Excitations*, Hirschegg, Austria (GSI, Darmstadt, 1999), p. 200.
[63] J. P. Bondorf, A. S. Botvina, and I. N. Mishustin, Phys. Rev. C **58**, R27 (1998).
[64] D. Stauffer and A. Aharony, *Introduction to Percolation Theory*, 2nd ed. (Taylor and Francis, London, 1992).
[65] H. Nakanishi and H. E. Stanley, Phys. Rev. B **22**, 2466 (1980).
[66] D. Stauffer, Phys. Rep. **54**, 1 (1979).
[67] J. B. Elliott *et al.*, Phys. Rev. C **62**, 064603 (2000).
[68] B. K. Srivastava, *Proceedings of the International Workshop XXVII on Gross Properties of Nuclei and Nuclear Excitations*, Hirschegg, Austria (Ref. [62]), p. 247.
[69] D. H. E. Gross, Phys. Rep. **279**, 119 (1997); *Proceedings of CRIS '96* (World Scientific, Singapore, 1996), p. 296.
[70] A. Hüller, Z. Phys. B: Condens. Matter **93**, 401 (1994).
[71] R. P. Scharenberg, *Proceedings of the International Workshop XXVII on Gross Properties of Nuclei and Nuclear Excitations*, Hirschegg, Austria (Ref. [62]), p. 237.
[72] S. Levit and B. Bonche, Nucl. Phys. **A437**, 426 (1985).
[73] M. D'Agostino *et al.*, Nucl. Phys. **A647**, 153 (1999).
[74] Ph. Chomaz and F. Gulminelli, Nucl. Phys. **A650**, 329 (1999).
[75] M. D'Agostino *et al.*, Phys. Lett. B **473**, 219 (2000).
[76] Ph Chomaz *et al.*, Phys. Rev. Lett. **85**, 3587 (2000).
[77] O. Mulken and P. Borrmann, Phys. Rev. C **63**, 024306 (2001).
[78] D. H. E. Gross, M. E. Madjet, and O. Schapiro, Z. Phys. D: At., Mol. Clusters **39**, 75 (1997).